Geophysical Journal International

Geophys. J. Int. (2011) **186**, 615–631 doi: 10.1111/j.1365-246X.2011.05076.x

New global seamount census from altimetry-derived gravity data

Seung-Sep Kim* and Paul Wessel

Department of Geology and Geophysics, University of Hawai'i at Manoa, 1680 East-West Road, Honolulu, HI 96822, USA. E-mail: seungsep@snu.ac.kr

Accepted 2011 May 9. Received 2011 May 9; in original form 2010 December 3

SUMMARY

Recent revisions to the satellite-derived vertical gravity gradient (VGG) data reveal more detail of the ocean bottom and have allowed us to develop a non-linear inversion method to detect seamounts in VGG data. We approximate VGG anomalies over seamounts as sums of individual, partially overlapping, elliptical polynomial functions, which allows us to form a non-linear inverse problem by fitting the polynomial model to the observations. Model parameters for a potential seamount include geographical location, peak VGG amplitude, major and minor axes of the elliptical base, and the azimuth of the major axis. The non-linear inversion is very sensitive to the initial values for the location and amplitude; hence, they are constrained by the centre and amplitude of the uppermost contours obtained with a 1-Eötvös contour interval. With these initial conditions from contouring, we execute a step-wise and fully automated inversion and obtain optimal model estimates for potential seamounts; these are statistically evaluated for significance using the Akaike Information Criterion and F tests. A logarithmic barrier technique is applied to ensure positivity of all seamount amplitudes. After automatic and manual inspections of the model parameters we estimate actual heights and basal ellipses of the inspected potential seamounts directly from the predicted bathymetry grid. In this study, we find globally 24 643 potential seamounts ($h \geq 0.1$ km) that are located away from continental margins; 8458 potential seamounts are taller than 1 km. Although our global estimate is significantly lower than predictions from previous studies, a first-order reconciliation of the size-frequency statistics obtained from those studies reveals that the previous counts are systematically overestimated. Because of the ambiguity of gravity signals due to small seamounts of $h < 1$ km and the overlap with abyssal hills, we estimate the global seamount census to lie in the 40 000–55 000 range. The seamount data from this study are accessible from http://www.soest.hawaii.edu/PT/SMTS.

Keywords: Inverse theory; Gravity anomalies and Earth structure; Geomorphology; Submarine tectonics and volcanism.

1 INTRODUCTION

Despite considerable post-World War II investments in ocean exploration (e.g. Chandler & Wessel 2008), vast areas of the ocean floor [e.g. ~90 per cent at 1 minute resolution (Becker *et al.* 2009) or ~70 per cent at 5 minute resolution (Wessel & Chandler 2011)] remain uncharted by surface ships. Given cost estimates of $\sim 10^{12}$ USD for a complete mapping with high-resolution multi-beam shipboard measurements (Vogt & Jung 2000), a global coverage of the Earth's underwater landscape at ~100 m resolution seems highly unlikely for the foreseeable future. Yet, at the more modest resolution of ~5–10 km, an alternative approach to studying the ocean bottom is available: sea-surface height measurements from orbiting satellites record spatial changes in the gravitational field mostly caused by the density contrast between water and bathymetric features. A global gravimetric view of the seafloor, thus, becomes accessible through satellite-derived gravity data (Haxby *et al.* 1983; Sandwell & Smith 1997; Andersen & Knudsen 1998; Sandwell & Smith 2009; Andersen *et al.* 2010). This marine gravity anomaly data set has provided uniform and dense data coverage over all oceans and has enabled researchers to investigate both remote bathymetric features unexplored by oceangoing expeditions (e.g. Lazarewicz & Schwank 1982; Cazenave *et al.* 1983; Watts & Ribe 1984; Mammerickx 1992; McAdoo & Marks 1992; Small & Sandwell 1994) as well as large-scale deep-seated geophysical phenomena (e.g. Haxby & Weissel 1986; McAdoo & Sandwell 1989; McNutt 1998).

Traditionally, seamounts have been defined as isolated, extinct or active underwater volcanoes rising more than 1 km above the surrounding seafloor (Menard 1964). Given rapid advances in marine technologies, this height limit has been adjusted to include volcanic constructs with heights as low as 50–100 m (e.g. Smith & Cann 1990; Behn *et al.* 2004). Whether small or large, seamounts play

*Now at: SEES, Seoul National University, 599 Gwanangno, Gwanak-gu, Seoul 151-747, South Korea.

important roles in a diverse range of natural phenomena. For instance, they can pose as obstacles to submarine navigation (e.g. BBC 2005) and affect the propagation of tsunami waves (e.g. Mofjeld *et al.* 2004). Seamounts also sustain diversified marine habitats (e.g. Pitcher *et al.* 2007; Clark *et al.* 2010) and even influence the global ocean circulation (e.g. Gille *et al.* 2004). Many older seamounts are covered by manganese crust, a potential mineral resource that one day may become economical to harvest (e.g. Friedrich & Schmitz-Wiechowski 1980; Grigg *et al.* 1987). Finally, the geographical and size-frequency distributions of seamounts are required to study the evolution of underwater volcanism through time and space (e.g. Wessel 2001). Consequently, it is of great importance to locate and characterize seamounts globally.

Because of differences in data sets and methodology, many researchers have arrived at different global assessments of seamounts (Craig & Sandwell 1988; Wessel 2001; Kitchingman & Lai 2004; Hillier & Watts 2007; Costello *et al.* 2010). Reviews of these methods and the uncertainties of the different approaches and estimates have been presented by other researchers (Calmant & Baudry 1996; Wessel *et al.* 2010). Given the uniform coverage of satellite altimetry, such remote-sensing data traditionally have been used to assess the global seamount population. However, the most-cited studies relied on early versions of the Geosat/ERS grids (v. 7.2) that are now almost 15 years old (Wessel & Lyons 1997; Wessel 2001). Furthermore, the methodology developed in the previous studies used a limited search of morphological attributes that could be extracted from the data. In this paper, we will use the recently released altimetry-based gravity data and present a new non-linear inversion method for seamount detection, discuss the development and limitations of our method, present a revised global seamount census, and finally compare our new estimates with those of previous studies.

2 METHODOLOGY

The vertical gravity gradient (VGG) grid is the geopotential data set derived from the altimetry measurements using a simple algebraic computation that requires neither spherical harmonics nor Fourier transforms (Sandwell & Smith 1997). Because VGG amplifies short-wavelength signals (such as observed over seamounts and fracture zones) and suppresses long-wavelength trends (e.g. those associated with flexure and hotspot swells), the VGG grid becomes more suitable than the free-air gravity (FAA) grid for finding small features such as seamounts (e.g. Wessel & Lyons 1997). Fig. 1 shows that gravity anomalies over two small seamounts (4 km apart and

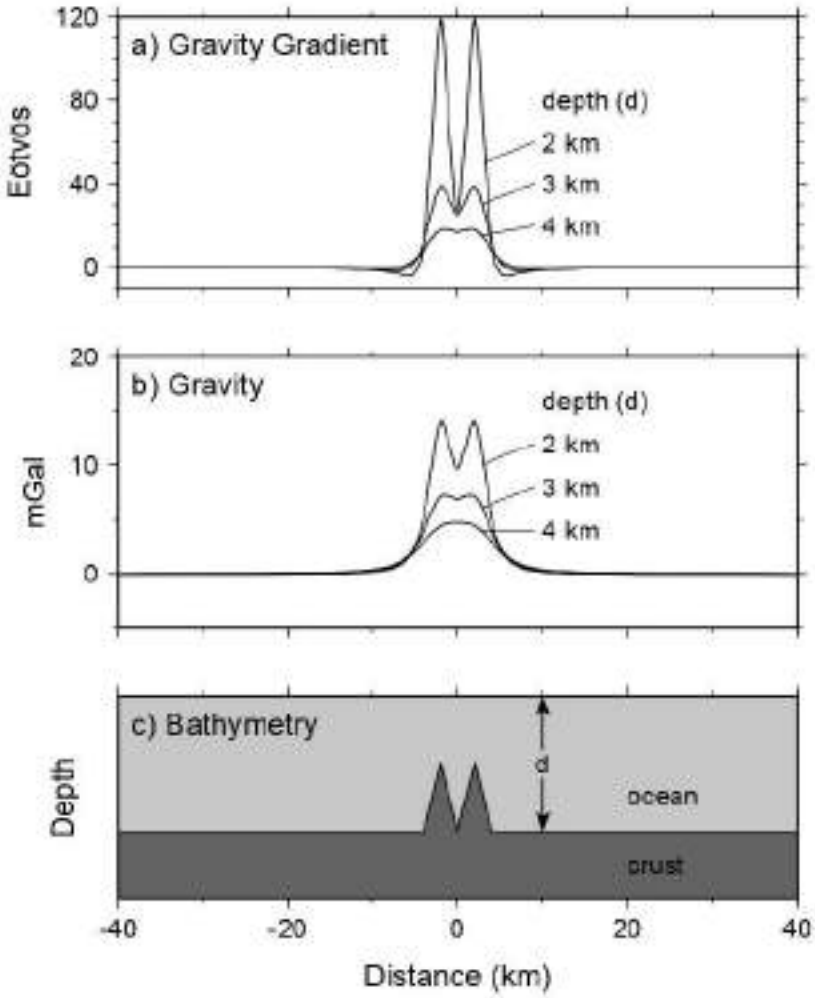

Figure 1. Limitation of topographic separation from gravity over closely spaced small seamounts. Two 1-km tall seamounts that are 4 km apart are considered for variable depths. While the gravity anomalies over the seamounts become indistinct when the regional depth exceeds the size of seamounts, the vertical gravity gradient anomalies stay separable. Modified from Wessel *et al.* (2010).

1 km tall) decay when the regional depth increases, while the VGG signals are separable for the two closely located seamounts. In addition, recent reprocessing of Geosat and ERS-1 altimetry data with a rigorous waveform retracking method has improved significantly both accuracy and resolution of the data (Sandwell & Smith 2005, 2009), which should significantly improve our chances of finding unmapped seamounts, especially those taller than 1 km. Therefore, we have utilized the 1-min Mercator VGG grid (version 16.1 at http://topex.ucsd.edu) to reassess the global seamount distribution (Sandwell & Smith 2009).

The coordinate system of the VGG grid is not conventional because gridding was performed in an equidimensional spherical Mercator map projection domain (Sandwell & Smith 1997), in which the grid cell dimensions are 1 arcminute (width) by 1 arcminute times the cosine of latitude (height). As a result, the number of grid cells per 1 arc degree increases with latitude, resulting in more data points towards the poles. If one simply projects this grid to the common geographical coordinate system, the original data points must be averaged for a cell with 1-min by 1-min dimension. This process dilutes the original resolution of the grid, preferentially at higher latitudes. Thus, to preserve the full resolution of the VGG grid, we performed our data processing and non-linear inversion directly in the Mercator domain and only projected our final estimates back to geographical coordinates.

2.1 VGG potential seamounts

High-resolution shipboard bathymetric mapping of seamounts has revealed a multiplicity of morphological forms, ranging from simple circular, truncated cones to complicated stellate shapes (e.g. Batiza & Vanko 1983; Rappaport *et al.* 1997; Mitchell 2001). While large seamounts ($h \geq 3$ km) are often reshaped by the development of rift zones and flank collapses that result in complex volcanic edifices (e.g. Ojin and Nintoku seamounts of the Emperor Seamount Chain, Smoot 1982), small ($h < 1$ km) and intermediate ($1 \leq h < 3$ km) seamounts tend to have single volcanic centres and display subcircular structures (e.g. Lamont Seamount Chain south of the Clipperton Transform, Fornari *et al.* 1988). Mitchell (2001) found that the transition from circular to stellate forms of seamount occurs gradually over a 2–4 km edifice height range, with the best transition estimate of 3 km height. Previous global seamount studies consistently show that the majority (>83 per cent) of detected seamounts are smaller than 3 km height (Wessel 2001; Hillier & Watts 2007; Wessel *et al.* 2010). Thus, we assume that an 'ideal' volcanic edifice is an elliptical truncated cone and anticipate that estimates based on this model will be adequate for most of the seamounts detected by our study, except for large seamounts with stellate form. Consequently, as most of the large seamounts have been mapped bathymetrically, we purposefully bias our modelling to be optimized for detecting and parametrizing the small and intermediate seamounts, which are more numerous than the large seamounts.

Gravity anomalies over seamounts observed at the sea surface are much smoother than bathymetry because the amplitudes of the gravity anomalies are attenuated exponentially with increasing depth to the seafloor, and this attenuation preferentially affects shorter wavelengths (Blakely 1996). Even if the volcanic edifice is a perfect cone, the gravity anomaly takes on a smoother (e.g. Gaussian-like) shape due to the attenuation. We take advantage of this 'upward continuation' phenomenon when searching for seamounts in the gravity data because a Gaussian shape can be expressed analytically and is easy to manipulate in both spatial and spectral domains. For example,

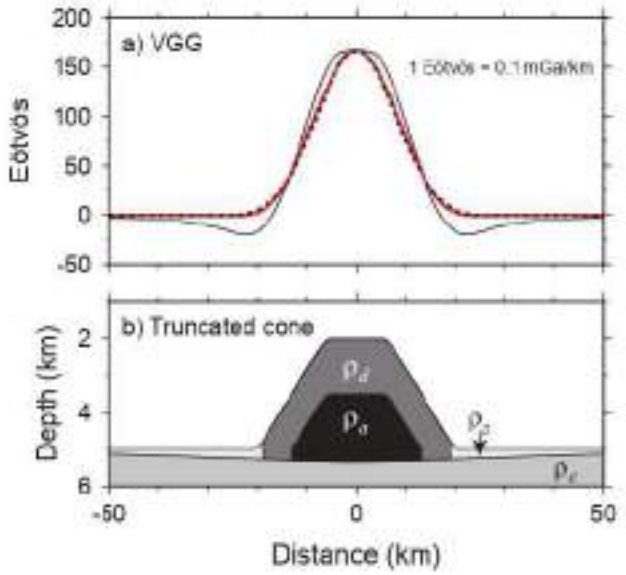

Figure 2. Polynomial seamount model. (a) The vertical gravity gradient (VGG) signal (black solid line) due to a truncated cone shown in (b) is approximated by the polynomial (red line) and Gaussian (black dotted line) seamount models. (b) Truncated cone with the dense core model (Kim & Wessel 2010). The densities of edifice (ρ_d), core (ρ_a), peripheral (ρ_c) and crust (ρ_c) are 2500, 2900, 2300 and 2900 kg m^{-3}, respectively.

Wessel & Lyons (1997) employed a circular Gaussian shape to approximate gravity anomalies caused by seamounts. In this approach, however, the distance to the first zero crossing (i.e. the radius of a seamount base) was assumed to equal the 3σ range that accounts for about 99.7 per cent of the area under the Gaussian function (since the curve never reaches zero). In contrast, we will utilize an elliptical polynomial model, R, which is similar to the Gaussian model but explicitly goes to zero at the seamount base (Fig. 2)

$$R(\mathbf{x}, \mathbf{x}_s, p, a, b, \theta) = \begin{cases} p\frac{(1+r)^2(1-r)^2}{1+r^4}, & |r| \leq 1 \\ 0, & |r| > 1 \end{cases}, \quad (1)$$

where $\mathbf{x} = (x, y)$ is the position vector, $\mathbf{x}_s = (x_s, y_s)$ is the summit location, and p is the peak amplitude. Then, the normalized radial distance from the summit, r, is defined as

$$r = \sqrt{A(x - x_s)^2 - 2B(x - x_s)(y - y_s) + C(y - y_s)^2} \quad (2)$$

with

$$A = \frac{1}{b^2}(f^2\cos^2\theta + \sin^2\theta)$$
$$B = \frac{1}{b^2}(1 - f^2)\cos\theta\sin\theta, \quad (3)$$
$$C = \frac{1}{b^2}(f^2\sin^2\theta + \cos^2\theta)$$

Here, $f = b/a$, where a and b are the major and minor semi-axes of the basal ellipse, respectively, and θ is the angle between the major and east–west (x) axes. A circular polynomial seamount can be simplified further with

$$r = \frac{\sqrt{(x - x_s)^2 + (y - y_s)^2}}{r_s}, \quad (4)$$

where r_s is the radius of the seamount base.

Fig. 2 demonstrates the similarity between the polynomial (red line) and Gaussian (black dotted line) models and compares these models with the VGG signal (black solid line) over a typical truncated cone. The dense core model (Kim & Wessel 2010) was employed to predict the free-air gravity anomalies (FAA) arising from the density differences and flexed crust (Fig. 2b). Then, the VGG signal was estimated by taking the vertical derivative of the predicted FAA data. There is little difference between the VGG shapes predicted using the Gaussian and parabolic models. However, the width of the VGG data estimated using the dense core model is wider than either model. Such differences depend on the mass distribution of the seamount implied by the truncation level, the ratio between its height and basal radius and the amount of flexure underneath the seamount. Predicting such details would require more geophysical information (e.g. bathymetry and seismic refraction profiles). Thus, the polynomial model serves as a simple approximation to typical VGG anomalies over seamounts.

Craig & Sandwell (1988) found that for the Gaussian seamount model the peak-to-trough distance of a single vertical deflection profile could be used to infer seamount diameter, and that this feature was insensitive to the cross-track location of the profile. However, for smaller seamounts this relationship becomes difficult to measure. While Craig & Sandwell (1988) could only use individual tracks due to the large track spacing, we have a gridded data set available based on a dense set of satellite tracks; hence we chose to fit the VGG data directly using the elliptical polynomial model.

Because seamounts are volcanic constructs, their gravity anomalies protrude upwards from the regional gravity level. In the following, we will describe how we fit the elliptical polynomial model to such protuberances in the VGG grid. Obviously, not all positive VGG bumps indicate the presence of seamounts since other tectonic features (e.g. abyssal hills and fracture zone scarps) can result in similar signals. Thus, we will first construct a set of 'potential' seamounts parametrized by the elliptical polynomial model and then apply statistical model selection criteria and both automatic and manual inspections in order to eliminate most unrealistic potential seamounts.

2.2 Non-linear inversion for elliptical polynomial seamounts

If a given domain has S elliptical polynomial seamounts, we can construct a non-linear least-squares problem for estimating the six parameters, $\mathbf{m} = (p, x_0, y_0, a, b, \theta)$, for each polynomial seamount by minimizing

$$E(\mathbf{M}_S) = \sum_{i=1}^{N} \left[\frac{V_i - R_i(\mathbf{M}_S)}{\sigma_i} \right]^2 - 2\gamma \sum_{j=1}^{5} \ln p_j, \qquad (5)$$

where N is the number of data points used for the fit, V_i is the observed VGG at the ith data point, and σ_i its standard deviation of data noise. Here, R_i is the predicted VGG at the ith data point using $\mathbf{M}_S = (\mathbf{m}_1, \mathbf{m}_2, \ldots, \mathbf{m}_S)$. Thus, the first term in eq. (5) is a standard chi-squared measure of misfit between the observed and predicted data. The second term is a positivity constraint on the amplitude parameters, p_j, with a logarithm barrier, γ (Li & Oldenburg 1996; Baptista *et al.* 2005). The logarithm term increases the gradient of the misfit if the amplitude keeps decreasing towards zero and hence ensures that solutions with negative amplitudes are avoided. A standard Levenberg–Marquardt approach is used to linearize and solve eq. (5) (Press *et al.* 1992).

2.3 Data noise and statistical model selection

Like other geophysical data, the VGG has noise due to measurement and theory errors. While the measurement error is due to instrumentation (e.g. range precision of altimeter) and ambient noise (e.g. ocean waves and tide model error), the theory error derives from the simplified parametrizations of Earth models and idealized treatment of forward problems (Sandwell & Smith 1997). To improve the accuracy of the recovered gravity field, researchers enhanced the range precision of the existing altimetry measurements by better constraining the sea surface slope errors (Maus *et al.* 1998; Sandwell & Smith 2005). As a result, the signal-to-noise ratio of the current VGG data (v. 16.1) has been improved more than 40 per cent from the previous release (v. 9.1; Sandwell & Smith 2009).

In addition to the data noise present in the VGG grid, our treatment introduces additional errors. Because eq. (5) does not include a complete set of parameters representing all geophysical phenomena captured in the VGG data (e.g. gravity signals due to abyssal hills, fracture zones, crustal and subcrustal density variations), the VGG signals not related to seamounts become our theory error. The elliptical polynomial model also contributes to the theory error as the model cannot handle completely the irregularity of VGG anomalies. In general, one can address this issue by adopting a more accurate model or by incorporating the measure of error correlations into the inversion formulation (e.g. Dosso *et al.* 2006). The former is the very reason we chose the elliptical polynomial model because it is a more appropriate model than the circular models used in previous studies (Wessel & Lyons 1997; Hillier & Watts 2007). However, developing a complete Earth model to explain every detail of the gravity field is impractical. Thus, we set an amplitude threshold ($p_{\min} = 10$ Eötvös) that the VGG amplitude of potential seamounts must exceed, by assuming that VGG peaks lower than this threshold would be more likely associated with data noise or small-scale geologic features (e.g. abyssal hills) than actual seamounts. This threshold is about twice the standard deviation of observed VGG anomalies in regions void of major geologic features (see insets in Fig. 3). In addition, we ameliorate the theory error further by performing regional-residual separation on the VGG grid and subject the seamount model to both automatic and manual inspections (Section 2.5).

However, error correlations are generally unknown and require reasonable assumptions about the data uncertainty distribution. A common approach is to assume that errors follow a Gaussian distribution and are spatially uncorrelated, which enables the use of σ_i in eq. (5) (i.e. a diagonal covariance matrix). Unfortunately, this approach becomes less effective in describing the data uncertainty distribution of the VGG grid because the errors in the raw altimetry measurements become correlated through data processing. In this case, one can estimate a full data covariance matrix with off-diagonal elements from the residual data (i.e. the observed data minus the predicted model) using an iterative procedure (Montgomery & Peck 1992; Dettmer 2006; Dosso *et al.* 2006). For our study, however, incorporating a full data covariance matrix into eq. (5) would be very expensive in terms of computation time because a $N \times N$ matrix would need to be inverted at each iteration as the model parameters get updated. In addition, the iterative approach has been successfully applied only to 2-D data sets (e.g. acoustic measurements at a hydrophone) and hence requires careful consideration for 3-D data (e.g. VGG grid). Neglecting the off-diagonal elements in eq. (5), therefore, may lead to underestimation of model-parameter uncertainties.

Here, we address the effect due to correlated errors by considering the following aspects. First, the uncertainties of the model parameters for VGG potential seamounts are not directly converted to uncertainties of the parameters for bathymetric ideal seamounts; that step involves additional forward modelling (e.g. Wessel & Lyons 1997). Several tests with synthetic noise and VGG seamounts also showed that the model parameters determined with a diagonal covariance matrix predicted the original parameters in a consistent manner. Thus, we use eq. (5) with a diagonal covariance matrix (i.e. single standard deviation) and regard the best model parameters for VGG potential seamounts as a first-order approximation of actual VGG anomalies. Second, the parameter affected most by correlated data is the number of potential seamounts (i.e. S). Because this parameter is not solved for by eq. (5), we constrain S using statistical model selection criteria. However, such statistical tests inherently assume that each measurement is independent, which is invalid for the VGG grid due to its correlated nature. As a first-order correction, we determine the effective number of uncorrelated data, N_E, based on autocovariance estimates of the VGG data and apply it to the model selection criteria.

We applied the indirect method of computing autocovariance estimates based on the Wiener–Khinchin theorem (Press *et al.* 1992) to two areas at different latitudes, where no significant geologic features were observed (Fig. 3). The 2-D autocovariance estimates were averaged over one radial pixel distance (i.e. the distance between two neighbouring grid points of the VGG data in the Mercator domain) to define the correlation length of the VGG data using the first zero-crossing of the radial covariance estimates. The correlation length at Equator (Fig. 3a) is ~8 km, while the high latitude case (Fig. 3b) is slightly better, at ~6 km. This may be because the track spacing is closer at higher latitude and hence the noise is lower (Sandwell & Smith 1997). The radial autocovariance estimates indicate that a VGG value at one grid node is strongly correlated with neighbouring VGG values located within a radius of 5 pixels. Thus, we estimated the effective number of uncorrelated data, N_E, as

$$N_E = N / C_E^2, \tag{6}$$

where the correlation pixel length, $C_E = 5$, as shown in Fig. 3.

Finally, we address the most important question of this study: How many VGG potential seamounts are necessary to optimally fit eq. (5)? Statistically, we can examine this question using model selection criteria (MSC) that tests if a model with $S + 1$ seamounts significantly improves the misfit relative to a model with only S seamounts. One of the applied MSC is the Unbiased Akaike information criterion (AIC_u) (Tsai & McQuarrie 1999) defined as

$$AIC_u = \ln\left[\frac{\sum_{i=1}^{N}(V_i - R_i(\mathbf{M}_S))^2}{N_E - M}\right] + \frac{N_E + M}{N_E - M - 2}, \tag{7}$$

Here, $M = 6S$ is the total number of the model parameters in $\mathbf{M}_S$. The first term in eq. (7) is a measure of the misfit with S seamounts. However, if S is overestimated for a given data set then AIC_u will be penalized by the second term (a measure of model complexity). Thus, $AIC_u(\mathbf{M}_{S+1})$ becomes less than $AIC_u(\mathbf{M}_S)$ if the improvement in misfit made by a model with one more seamount, $\mathbf{M}_{S+1}$, is statistically significant. The other criterion considers the F-ratio test (Stein & Gordon 1984), that is

$$F = \frac{\left[\chi^2(\mathbf{M}_S) - \chi^2(\mathbf{M}_{S+1})\right]/(M_{S+1} - M_S)}{\chi^2(\mathbf{M}_{S+1})/(N_E - M_{S+1})}, \tag{8}$$

where M_S is the number of model parameters for S seamounts and the chi-squared function is the same as the first term of eq. (5). This F-statistic is tested against $P_{0.95}(n_1, n_2)$ with $n_1 = (M_{S+1} - M_S)$ and $n_2 = (N_E - M_{S+1})$, for a 95 per cent confidence level. Although both methods tend to result in the same statistical outcome, we conservatively only accept a model that passes both tests. Using the above MSC, therefore, we arrive at the number of potential seamounts that are statistically significant for the given VGG data with correlated noise.

2.4 SeaHunt: automated global seamount search

We first removed long-wavelength signals from the VGG data by applying a spatial median filter with a 400 km filter width because such regional variation is not directly associated with the seamounts

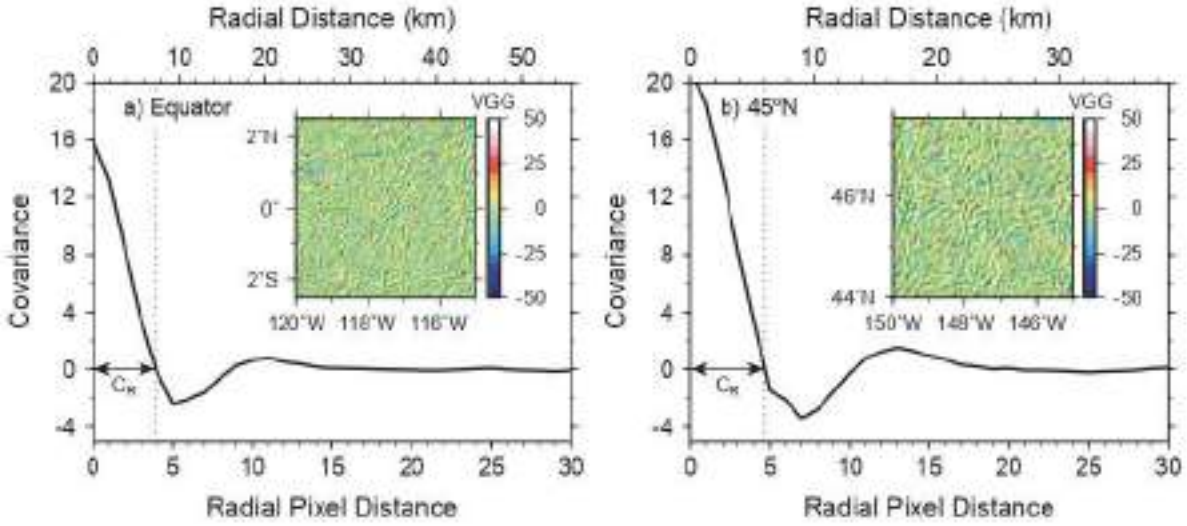

Figure 3. Correlation length of the VGG 16.1 grid. (a) Radial covariance estimate of the VGG grid at Equator (inset). The examined area has a mean of 0 Eotvos and a standard deviation of 5.8 Eotvos. (b) Radial covariance estimate of the VGG grid at ~45°N (inset). The examined area has a mean of 0.1 Eotvos and a standard deviation of 6.6 Eotvos. Correlation pixel length, C_E, is the distance to the first zero crossing of the covariance estimates. Because these two areas do not have any large-scale geologic features, we use the standard deviations of these regions to determine the amplitude threshold, p_{crit}.

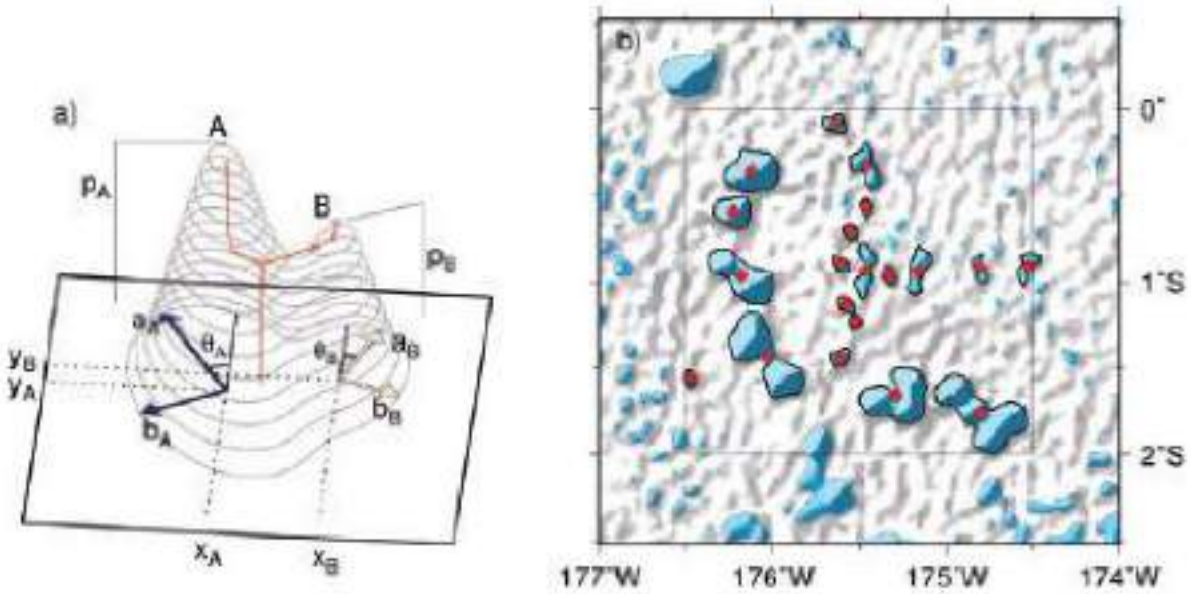

Figure 4. Contouring and base polygons. (a) Schematic diagram of contouring when two VGG potential seamounts with different amplitudes are considered; see text for details. The model parameters are denoted for the potential seamounts, A and B. (b) Base polygons inside the small inversion box (thin solid line), which is designed only for demonstration purpose. The actual inversion box is 5° × 5° as discussed in text. The coloured areas indicate VGG exceeding the threshold (p_{cut} = 10 Eötvös), while those outlined by dashed lines are larger than the area threshold (50 km^2). The red diamonds are the centres of basal ellipses fitted to the base polygons. Thus, we choose the base polygons (thick solid line) by examining whether their centres are inside a given inversion box.

themselves (Smith 1990, Wessel & Lyons 1997). The residual VGG grid obtained by subtracting the regional (i.e. filtered) VGG data from the original data was used for the subsequent processes.

Among the six model parameters (see Fig. 4a), the misfit is most sensitive to the location and VGG amplitude of a polynomial seamount, that is (x_o, y_o, p). Thus, we contoured the residual VGG data using a 1-Eötvös interval and kept track of each contour, because seamounts produce positive gravity signals and consequently their locations and amplitudes determine the geometry of those contours (Fig. 4).

As an example (Fig. 4a), if a given area has two seamounts (the VGG peak of seamount A is larger than that of seamount B), the contouring returns the first closed polygon at the summit of seamount A. Whenever a new polygon is generated, the process estimates its area and determines a best-fitting ellipse to that polygon, which usually has an irregular shape. This step parametrizes all polygons (i.e. contours) generated and enables us to recover these geometrical parameters at any contour level. As contouring proceeds, it tests if a new polygon encompasses the previous polygons. When the contouring reaches the summit of seamount B, the process results in two distinct polygons: one is from seamount A and the other is the first polygon due to seamount B. Because the latter does not include any of the previous polygons from seamount A, the contouring can recognize this event from the above test and maintain the polygon set of seamount A separately from that of seamount B, assigning unique identification numbers to each set. At each interval, we progressively construct a database of the area of a closed contour, its centre location, major and minor axes, and the azimuth of the best-fitting ellipse to that contour. More importantly, the contouring gives us a maximum number of potential seamounts in a given area because the first-contour of each unique polygon set is associated with a positive VGG bump that *may* result from an actual seamount. Thus, an initial parameter set can be constructed by using the centres (x_c, y_c) of best-fitting ellipses for the first contour level, p, for each feature.

For our global seamount analysis, we divided the Earth into 25 plate-size domains based on a digital model of plate boundaries (Bird 2003) by merging relatively smaller plates with their nearest neighbour plates (Table 1) and generated 5° × 5° boxes (called inversion boxes) that filled any given plate-size domain entirely. For each plate-size domain, we carried out the contouring at the specified interval (i.e. 1 Eötvös) down to the amplitude threshold (p_{cut} = 10 Eötvös). We used the p_{cut} contours as base polygons, inside which potential seamounts, if any, must be found. To reduce the number of spurious base polygons we only retained polygons whose area exceeded 50 km^2 (i.e. area threshold based on the correlation analysis of the VGG grid; section 2.3). The area threshold can include multiple seamounts of elevation 100 m, however the VGG grid used for our study does not have sufficient resolving power to differentiate them without independent measurements (i.e. shipboard soundings). This analysis yielded 415 710 initial candidates for potential seamounts.

The initial parameters (x_o, y_o, p), given by the slicing process are good initial choices for the location and VGG amplitude of potential seamounts (Fig. 5a), while the other parameters, (a, b, θ), need to be determined directly by minimizing eq. (5). However, this non-linear system quickly becomes unstable if initial guesses for the parameters (a, b, θ) are too distant from the actual values. Thus, we constructed a step-wise inversion that solves eq. (5) using the circular polynomial model (Fig. 5b) and then refines the circular parameters to yield an elliptical polynomial model (Fig. 5c). In addition, we parallelized the inversion since the model parameters optimized for one box are independent from those of other boxes. The inversion search with applied model selection criteria resulted in 110 127 potential seamounts.

2.5 Automatic and manual inspections

As the VGG grid is derived from the sea surface height measurements, it becomes discontinuous over large subaerial landmasses.

Table 1. Number of seamounts identified for each plate-size domain. Seamount density is the ratio of seamount counts to the area of plate-size domain. The plate notations are from Bird (2003), except for the plate-size domains consisting of combined plates.

Plate-size domain	$h \geq 1$ km	Total ($h \geq 0.1$ km)	Density (10^{-6} km^{-2})
AF	857	3888	41.72
AN	639	4837	38.09
AO[a]	820	2855	34.73
AR	6	47	4.59
CI[b]	59	149	18.03
CO	40	185	33.42
CP[c]	1	1	0.16
EA	3	9	26.67
EU	76	532	5.42
GP	0	2	26.98
IN	99	356	16.79
JF	0	21	25.52
JZ	7	40	155.22
NA	182	705	3.50
NZ	440	1112	41.55
OA[d]	2	7	0.24
PA	4055	6863	44.97
PSM[e]	419	697	57.72
RI	2	30	103.00
SA	373	1133	15.84
SC	37	134	39.84
SD[f]	39	80	4.39
SO	281	924	28.93
SW	21	36	114.49

[a] Includes AU, CR, KE, NI, BR, FT, NH and TO plates.
[b] Includes BH, MN, NB, SS, CL, MO, SB and WL plates.
[c] Includes CA and PM plates.
[d] Includes AM, ON, OK and YA plates.
[e] Includes MA and PS plates.
[f] Includes BS, MS, TI, BU and SU plates.

Although a complicated gridding scheme is applied to fill the altimetry data gaps and produce the VGG grid (Sandwell & Smith 2005), the VGG data over continents and large islands (e.g. New Guinea) are poorly constrained. Especially, the altimetry data near continental margins are strongly correlated with oceanographic signals (e.g. tidal waves and upwelling currents) and reflect non-volcanic geologic processes (e.g. sedimentation and erosion), which can be similar to VGG anomalies from seamounts. Another important aspect is that volcanic seamounts are unlikely to exist along continental margins. Thus, we defined Seamount Exclusive Zones (SEZs) using the 2000 m isobaths obtained from ETOPO2v2 (NGDC 2006). The seamounts found inside or within 20 km distance from the SEZs (black lines in Fig. 8) were automatically tagged for exclusion from the list of potential seamounts. The 20 km distance criterion was added because the constant isobaths were not sufficient to tag seamounts near the continental margins systematically and effectively.

The model parameters estimated by our automated method can be biased because of the theory error, which results from the inability of the model to predict data noise and non-seamount-related signals; both effects tend to overestimate the major axis. By extending the major axes of small potential seamounts (usually with $p <$ 30 E0v0s), the model may be able to reduce the misfits in areas where the VGG grid is complicated by roughness of the seafloor (e.g. the Southwest Indian Ridge) and where linear trends are apparent (e.g. near fracture zones). We automatically tagged potential seamounts with unrealistic major axes if the major-to-minor axes ratio was less than 0.2 (i.e. $f \leq 0.2$) and if the ratio of the major axis to the VGG amplitude was larger than 0.7 (i.e. $a/p \geq 0.7$). We derived these empirical and conservative conditions based on our extensive data analysis of the identified potential seamounts with known seamounts constrained by shipboard bathymetry and then applied them to exclude unrealistic potential seamounts.

First, we validated the detected potential seamounts over several test areas with complete bathymetric coverage (e.g. the Geologists Seamount Group, Foundation Seamounts, and Rano Rahi Seamount Field) and found no false detections. Next, we compared the potential seamounts to the VGG, FAA, and predicted bathymetry (TOPO 12.1) grids using Google Earth. Despite our automatic tagging, we still had to tag manually multiple peaks over flat-topped seamounts, stellate seamounts, and large islands, as well as peaks detected at volcanic ridges and over rough bathymetry, because we could not find any systematic relationship between our model parameters and the VGG over such morphologies. For example, a truncated seamount (e.g. guyot) exhibits FAA variation over the summit and the slope of the FAA depends on the flatness of the truncated seamount and its density structure. The VGG derived from such a flat FAA field may have multiple local maxima for each seamount, which consequently cause the contouring to produce multiple initial peaks for such single seamounts. For most cases, the MSC was effective in merging them into one summit, but not for large guyots (e.g. Pallada Guyot). As anticipated at the model building stage, the MSC was not adequate to exclude initial peaks obtained at flanks of stellate seamounts, large islands and at volcanic ridges (e.g. Necker ridge). These multiple peaks were therefore tagged via a manual inspection. While we strived for consistency in making these decisions, it is nevertheless clearly a subjective procedure.

Finally, we tagged islands based on distance to the nearest coastline. A volcanic island is a seamount rising above the sea surface. However, its exposed area above the sea surface varies considerably. Some islands exhibit large subaerial surfaces with high elevations, while others have small areas barely above sea level (e.g. atolls). In addition, the gravimetric centre of a volcanic island is not always the same as the centre of the subaerial surface. Due to these variations, no systematic approach to find islands was made. Instead, we define an island if the distance to the nearest coastline from any subaerial point of the island exceeds 4 km. It means that the length between the two closest ends of the island is longer than 8 km. Given the VGG correlation length of ~8 km (Fig. 3), data gaps longer than 8 km cannot be constrained through nearby altimetry data points. Using this criterion, we could tag 62 islands from the manually inspected potential seamounts. After removing all tagged potential peaks from the list, we arrived at 25 721 potential seamounts.

2.6 Seamount height estimation

The model parameters of the identified VGG potential seamounts can be used for various studies: spatial distribution of seamounts (Craig & Sandwell 1988; Wessel & Lyons 1997), plate tectonic reconstructions (Jarrard & Clague 1977), and refining absolute plate motions (Wessel & Kroenke 1997). The amplitude and basal ellipse parameters of the VGG potential seamounts, however, cannot be translated linearly to obtain actual dimensions and volumes of bathymetric seamounts, which are desirable when investigating intraplate volcanism (Wessel 2001; Watts *et al.* 2006; Hillier 2007). To address this problem one can use either the predicted bathymetry from gravity (Jung & Vogt 1992; Sichoix & Bonneville 1996; Ramillien & Cazenave 1997; Smith & Sandwell 1997; Ramillien

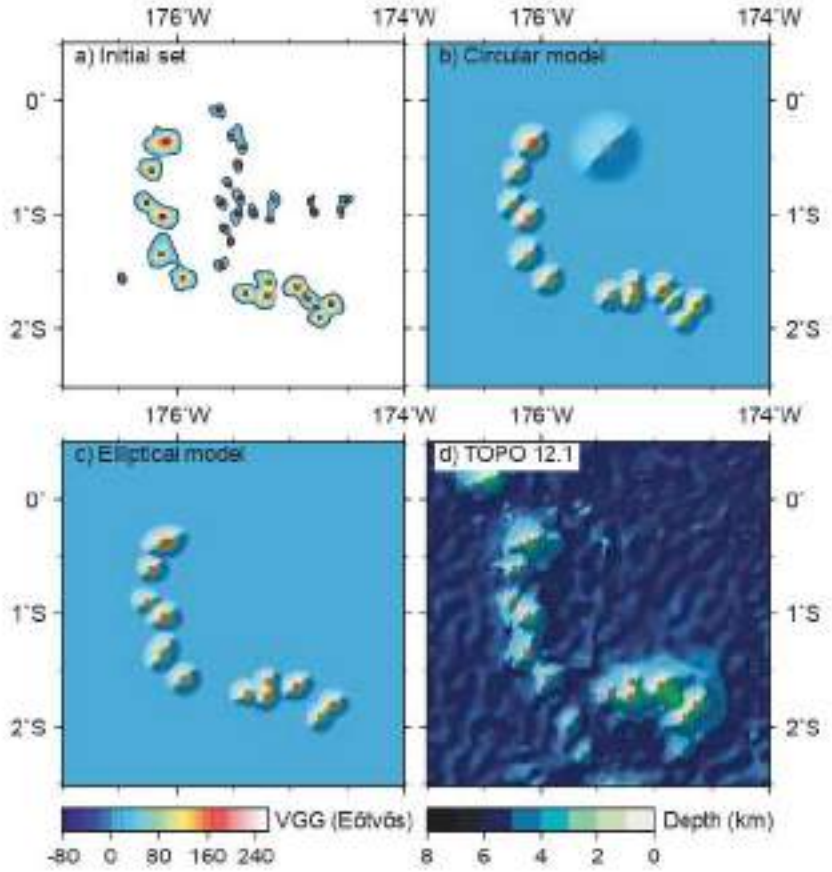

Figure 5. Automated step-wise inversion for seamount searching. (a) The initial data set consists of the VGG data inside the base polygons and the initial model parameters, (x_o, y_o, p), prepared by contouring (see Fig. 4). The potential seamount locations are indicated by the red squares. (b) Circular polynomial model. The model selection criteria (MSC) are applied to identify statistically significant potential seamounts (red squares) using the circular polynomial model. (c) Elliptical polynomial model. The elliptical polynomial model is applied to approximate the given VGG data. (d) The identified potential seamounts are compared with the predicted bathymetry, TOPO 12.1.

& Wright 2000) or a separate modelling scheme (Baudry *et al.* 1987; Calmant 1994; Wessel & Lyons 1997). Both methods to predict seamount heights suffer from a common error source due to the densities used for seamounts (Ribe 1982; Dixon & Parke 1983; Baudry *et al.* 1987; Baudry & Calmant 1991). In addition, the global bathymetry data were estimated on assumption of a constant elastic thickness; the height prediction can be biased, especially for large seamounts that were formed recently relative to the thermal age of the lithosphere beneath them (i.e. young seamount on old crust; Dixon *et al.* 1983). To remedy such bias, Wessel & Lyons (1997) estimated the height parameter from a simplified forward modelling that considered a broad range of elastic thicknesses. They assumed the seamount had a Gaussian shape and built a look-up table for a wide range of heights and flank slopes in order to relate their gravimetric parameters (i.e. VGG and FAA amplitudes and VGG zero-crossing distance) to the height and radius of the seamount model. However, the uncertainty of the predicted height is greater for the small ($h < 1$ km) and intermediate ($1 \leq h < 3$ km) seamounts than for the large seamounts ($h \geq 3$ km) because the flexural signals due to the smaller seamounts ($h < 3$ km) are inherently less significant than those due to the large seamounts (Wessel & Lyons 1997). Thus, the uncertainty of the height parameter for the smaller seamounts predicted without bathymetry becomes similar in both approaches. For the large seamounts, the simple seamount model becomes inadequate because of their stellate form; however many of these have been mapped bathymetrically. In this study, therefore, we obtain the bathymetric parameters (i.e. actual height, major, and minor axes) for the VGG potential seamounts from the predicted bathymetry, TOPO 12.1 (Smith & Sandwell 1997), because it includes shipboard measurements wherever available.

As seen in Fig. 6(a), the basal ellipse (black solid line) of a seamount's VGG anomaly is generally narrower than the actual basal ellipse of the corresponding bathymetry. To estimate the height, we discretely scaled the basal ellipse of the VGG anomaly by 0.5, 2, 3 and 4 (see the concentric ellipses in Fig. 6a). For each scale we computed the median of the depths sampled at the four positions where the major and minor axes intersect the basal ellipse (see the red and black dots in Fig. 6a). The height estimate for each seamount is summit depth (black square in Fig. 6a) minus the median depth. Then, we compared five different height estimates and chose the height only when the examined scale resulted in a 50 per cent increase in height over the previous estimate (Fig. 6b). In Fig. 6, the height estimate is increasing continuously with scaling; however, the height is not increased by more than 50 per cent for scales larger than 3. Although this ratio constraint prevents excessive stretching and enables us to construct less overlapping basal ellipses (Fig. 7), we anticipate that the height estimates for seamounts of $h > 4$ km may be underestimated by ~15 per cent. Based on the estimated heights, we found 24 643 potential seamounts taller than 100 m out of 25 721 VGG seamounts.

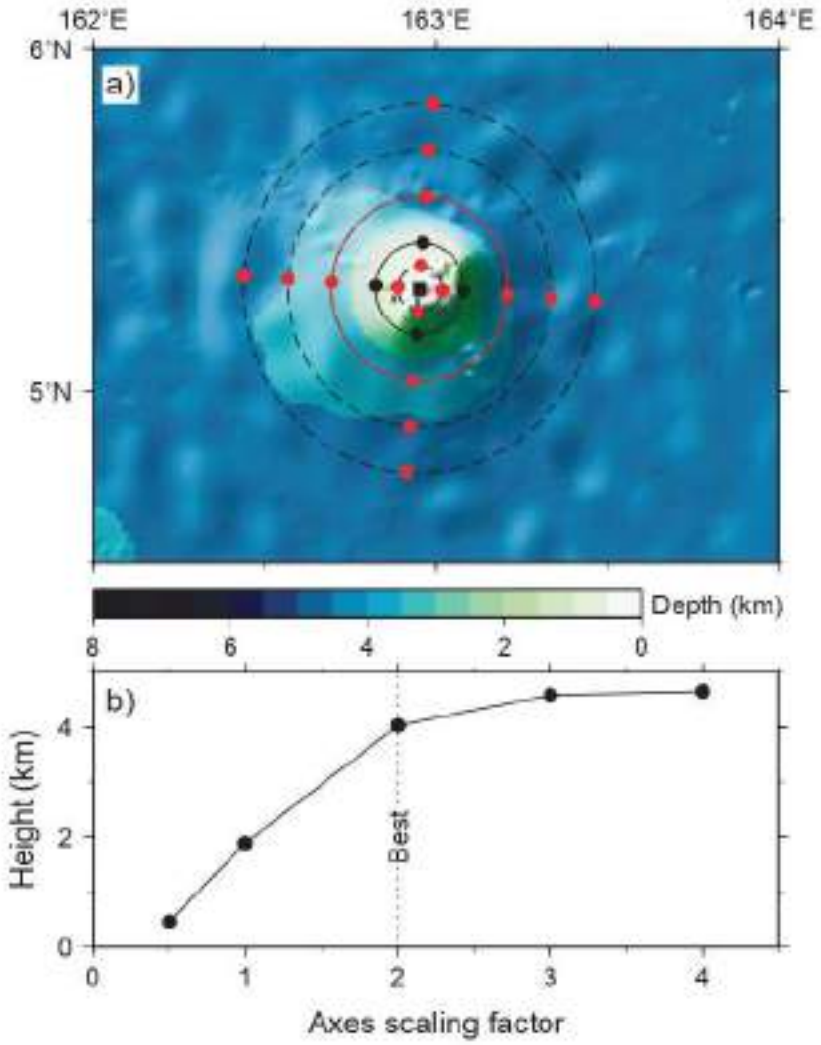

Figure 6. Height estimation from the predicted bathymetry grid, TOPO 12.1 (Smith & Sandwell 1997). (a) Scaled basal ellipses. The basal ellipse of the VGO potential seamount (black solid line) is scaled discretely by 0.5, 2, 3 and 4 (dashed and red concentric ellipses). The depths are sampled from the intersecting points between the major and minor axes and the ellipses (black and red dots). (b) Height estimation curve. The height is estimated by subtracting the regional depth (i.e. median value of the four depths from each scaled ellipse) from the summit depth [black square in (a)]. The best scale is determined if the height at that scale is increased more than 50 per cent relative to the previous height.

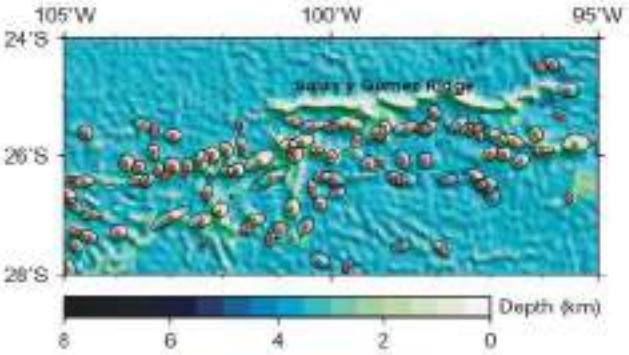

Figure 7. Bathymetric basal ellipses of potential seamounts scaled by the height estimation process. The locations (red dots) of potential seamounts are shown for a section of the Easter Seamount Chain. As discussed in the text, the Salas y Gomez Ridge at 25°S was manually excluded from the list of the potential seamounts.

3 RESULTS

The total of 24 643 potential seamounts taller than 100 m was determined and characterized by the processes described above; this is almost twice the number identified in the previous study (Wessel 2001). However, the term 'seamount' has been defined inconsistently in various studies due to the specific interests in a field of research or limitations of the data used in a study (Menard 1964; Jordan *et al.* 1983; White *et al.* 1983; Wessel & Lyons 1997; Wessel *et al.* 2010). A recent attempt to include diverse views on seamounts within multidisciplinary research communities describes seamounts as 'any geographically isolated topographic features on the seafloor taller than 100 m, including ones whose summit regions may temporarily emerge above sea level, but not including features that are located on continental shelves or that are part of other major landmasses' (Staudigel *et al.* 2010). The automatic tagging within the SEZs, the manual tagging of volcanic ridges, and the height threshold make our potential seamount count more compatible with modern terminology than those of previous studies. Although we

tagged 62 islands, our final seamount count still includes some small islands because the shortest width of their subaerial area is narrower than the 8-km VGG correlation length.

The spatial distribution of potential seamounts from this study (Fig. 8) shows that seamounts taller than 1 km (blue and red dots, $n = 8458$) generally occur in clusters, seamount chains, and arc regions, while large portions of seamounts less than 1 km (black dots, $n = 16185$) are located near mid-ocean ridges. This partitioning suggests that the intermediate and large seamounts are formed by mid-plate volcanism (e.g. mantle plumes), while the small seamounts are produced in near-ridge environments (Wessel 2001; Hillier 2007). A histogram of the height distribution of the seamounts (see inset in Fig. 8) also illustrates that the population of small seamounts ($h < 1$ km) is about twice that of intermediate and large seamounts ($h \geq 1$ km).

The Pacific Plate supports ~28 per cent of the identified potential seamounts. However, nearly half of the world's seamounts taller than 1 km are found on the Pacific Plate (Table 1), which confirms earlier results for the western Pacific (Craig & Sandwell 1988; Wessel & Lyons 1997; Hillier 2007). Following the Pacific Plate, numerous seamounts are found on the Antarctica, Africa, Australia, South America and Nazca plates. The rest of the intermediate and large seamounts ($h \geq 1$ km) are distributed over the Africa, Australia, Antarctica, and Nazca plates. Unlike the Pacific, the small seamounts ($h < 1$ km) on the Antarctica Plate make up more than 80 per cent of the seamounts for that plate. Although the seamount counts for the Philippine, Mariana and Sandwich plates are small relative to the global number of seamounts; nearly 60 per cent of seamounts found on these plates are taller than 1 km. It may imply that arc volcanoes can grow taller than near-ridge volcanoes due to the relatively static magma source supplied from the subduction process and the larger strength of an older plate.

3.1 New global seamount census

The total number of seamounts for a specific plate or the entire Earth has been one of the core questions that previous studies have tried to answer, regardless of variable data coverage (incomplete or complete) and methodologies (manual or automatic; e.g. Batiza 1982; Jordan *et al.* 1983; Abers *et al.* 1988; Wessel 2001; Hillier & Watts 2007). As complete mapping of all seamounts has yet to be made, the general approach to compensate for uncounted seamounts has been statistical extrapolation. This approach assumed that the height-frequency distribution follows either an exponential or power-law curve. Based on the choice of curve, the total number of seamounts for a region of interest could be fluctuating widely.

For instance, Wessel (2001) used a power-law relationship for the detected potential seamounts in the 2–7 km height range and predicted there might be 100 000 seamounts globally that are taller than 1 km. This number has been revised recently to 125 000 seamounts with an uncertainty range of 45 000–350 000 (Wessel *et al.* 2010); however, the same power-law condition was used. The revised power-law height-frequency distribution also predicted 25 million seamounts taller than 100 m, but might range from 8 to 80 million. This power-law curve is a straight line in a log-log plot, and the linear trend of the PW data (Wessel 2001) in the 2–7 km height range is well described by this empirical curve (PW; blue open squares in Fig. 9).

Hillier & Watts (2007) corrected their seamount counts to compensate for the sparse data coverage of ship-tracks and arrived at global predictions of 39 000 seamounts of $h > 1$ km (HW; grey open triangles in Fig. 9). They demonstrated that no single empirical curves are adequate to describe seamount abundances over the entire height range. This finding is also directly applicable to our height-frequency curve (KW; red circles in Fig. 9), which has

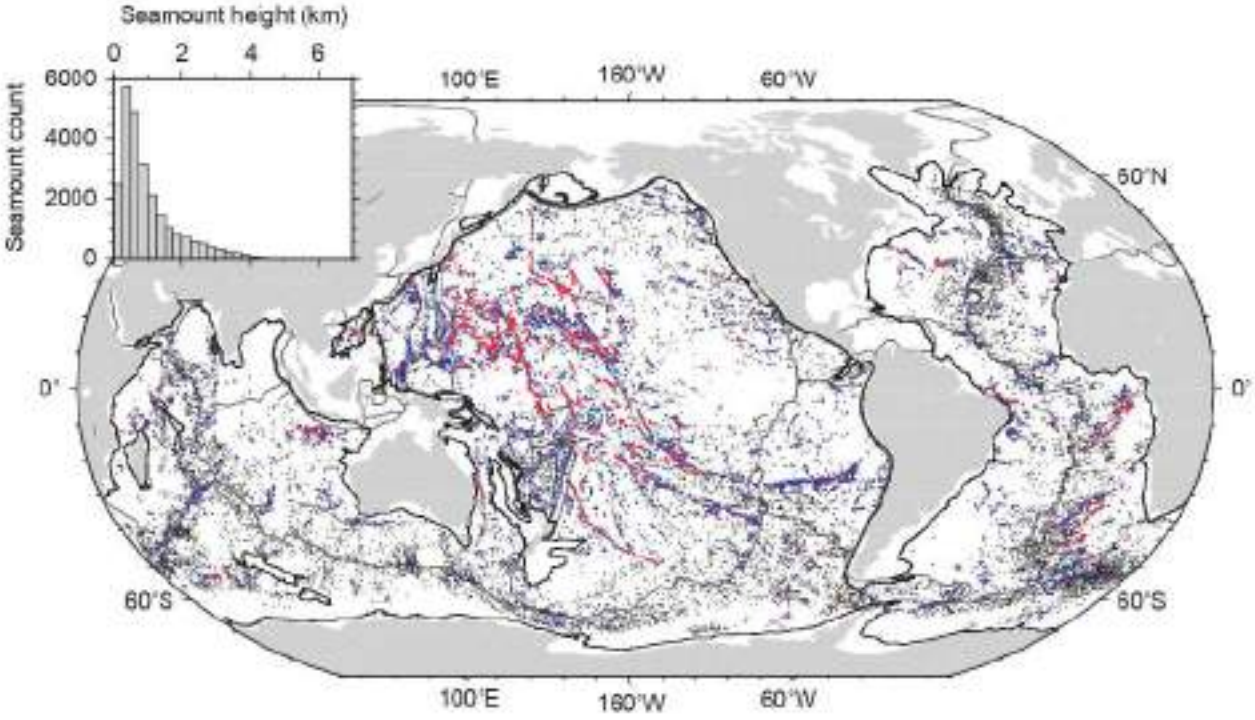

Figure 8. Global distribution of 24 643 potential seamounts identified by this study. Black dots for $0.1 \leq h < 1$ km ($n = 16\,185$), blue dots for $1 \leq h < 3$ km ($n = 7514$), and red dots for $h \geq 3$ km ($n = 944$). The plate boundaries (Bird 2003) are shown as grey lines and the Seamount Exclusion Zones (SEZs) defined by the 2000 m isobaths are drawn as black lines. Inset shows histogram of height distribution of potential seamounts.

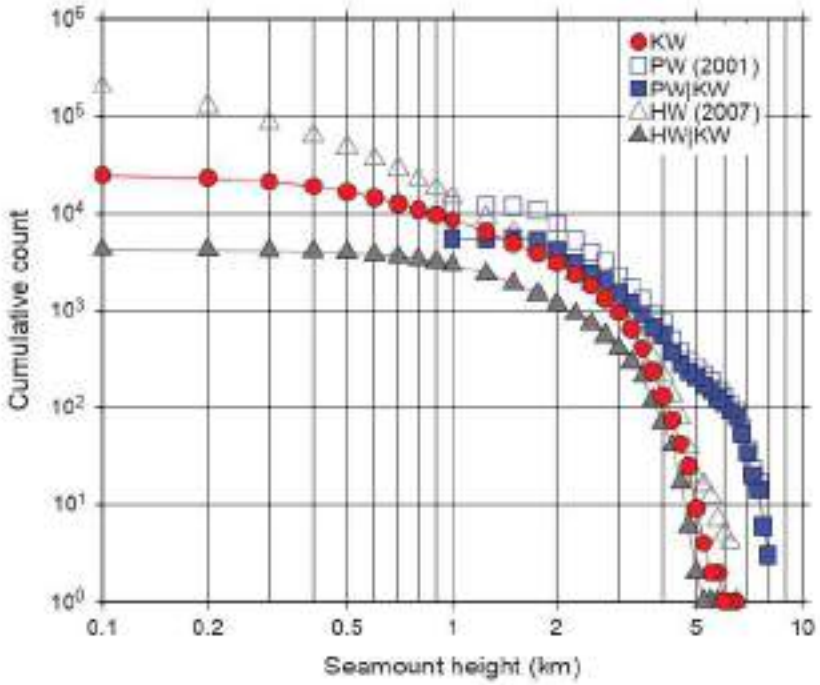

Figure 9. Height-frequency distributions of potential seamounts from KW (this study; red dots), PW (Wessel 2001) (blue open squares), reconciled PW (PW | KW; blue squares), HW (Hillier & Watts 2007) (grey open triangles) and reconciled HW (HW | KW; grey triangles). The curvatures of the distributions are maximized at ~3 km.

its maximum curvature at ~3 km and coincides (perhaps fortuitously?) with the transition height between circular and stellate seamounts (Mitchell 2001). Nonetheless, Hillier & Watts (2007) estimated 3 million seamounts ($h > 100$ m) using the power-law curve.

In this study, we predict a new global seamount census based on the identified seamount distribution and the age of seafloor. First, we constrain the upper limit for the seamounts of $h > 1$ km. Because our method finds 8458 potential seamounts of $h > 1$ km globally, if we consider the 62 counted islands and possible missing seamounts due to the SEZs, we can speculatively increase this number up to 10 000. We think that this count for the seamounts of $h > 1$ km is a reasonable upper limit because the SEZs can exclude only 217 seamounts from the PW data and 1131 seamounts from the HW data.

To estimate a global census of small seamounts ($0.1 \leq h < 1$ km), we need to consider the attenuation of gravity anomalies with increasing regional depths (i.e. upward continuation). As illustrated in Fig. 1, the VGG amplitudes of small seamounts situated at greater depths can become indistinguishable from the noise and VGG signals arising from other geological constructs (e.g. abyssal hills and faulted blocks). Due to such ambiguity of gravity signals and the non-statistical height-frequency model, we speculatively estimate the 'true' number of seamounts globally by assuming that the seafloor is uniformly covered by small seamounts. Geologically, small seamounts are formed on young lithosphere near mid-ocean ridges (e.g. Smith & Cann 1990). This fact alone increases the detectability of these young seamounts because the regional depth near the spreading ridges is typically shallower than other parts of the oceans (Parsons & Sclater 1977; i.e. less upward continuation) and

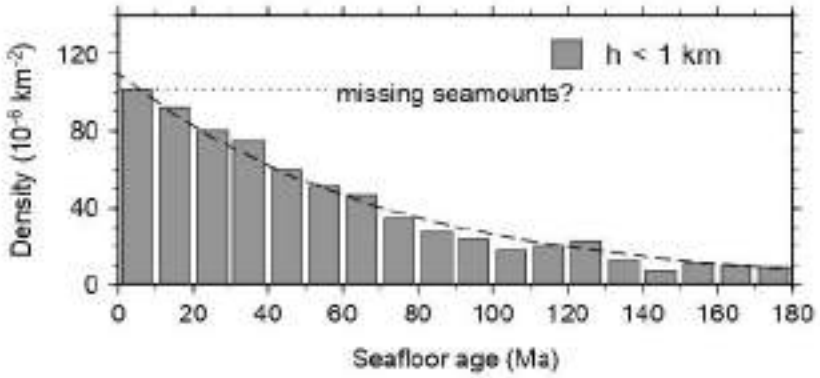

Figure 10. Seamount density for small seamounts ($0.1 < h < 1$ km) as a function of seafloor age. The seamount density (i.e. the ratio of seamount counts to seafloor area for each age bin) decreases for older seafloor, indicating small seamounts are likely to be undercounted because their gravity signals are subdued due to greater water depth and thick sediment coverage (see dashed curve). Crustal ages are sampled from the age grid 3.2 (Müller *et al.* 2008).

the near-ridge areas have the least sediment cover (Divins 2009), and hence the confidence level of our count for small seamounts on the youngest seafloor is relatively higher than that for the older seafloor (Fig. 10). If we can assume that the seafloor produced for any given geologic time period has experienced a constant seamount volcanism, a given area of the seafloor will have a constant seamount density (Fig. 10). If the seamount density of the youngest plate (< 10 Ma) is a proxy for the 'true' area coverage of small seamounts produced per 10 Myr for any geologic time period (Fig. 10), we can predict that there are ~30 000 small seamounts globally. If we impose a 50 per cent uncertainty to the observed seamount density of the youngest plate, the predicted count for seamount seamounts becomes ~45 000. This leads to a new global seamount census ($h \geq 0.1$ km) that ranges from 40 000 to 55 000. Of course, many of these smaller seamounts would be buried by sediments but could still give rise to a diminished gravity anomaly.

Nonetheless, the resolution of gravity is inherently limited by upward continuation. A chain of the small seamounts ($h < 1$ km), thus, may be identified as a single elongated seamount by our methods. The example of Fig. 1 illustrates such a possibility because the VGG amplitude over closely spaced seamounts is larger than the threshold of this study, yet the shape of the VGG data appears as a blanket over them. For such cases, shipboard bathymetry is preferable.

Finally, we can assess to what extent potential seamounts have been mapped by surface ships. The histograms in Fig. 11 show the ship data coverage per potential seamount by calculating Δs, the ratio of the number of shipboard measurements to the total number of gridpoints inside the basal ellipse. The TOPO 12.1 grid has embedded information on whether a gridpoint is constrained by shipboard bathymetry or interpolated by the standard prediction (Smith & Sandwell 1994). Only 24 per cent of the identified seamounts have more than 10 per cent coverage of shipboard bathymetry (Figs 11a and b), while ~40 per cent of the potential seamounts have no ship coverage. The bathymetric coverage also differs for the size of seamounts (Fig. 11c). About 90 per cent of the small seamounts ($0.1 \leq h < 1$ km; black) have less than 10 per cent ship coverage, while about 70 per cent of the intermediate ($1 \leq h < 3$ km; blue) and large ($h \geq 3$ km; red) have the same coverage. However, the bathymetric coverage for the intermediate and large seamounts is quickly improved because they are easy to locate. To chart these poorly constrained seamounts effectively, one may use our seamount database to plan a survey or transit so that a survey ship can pass over one of these seamounts by design (Sandwell & Wessel 2010).

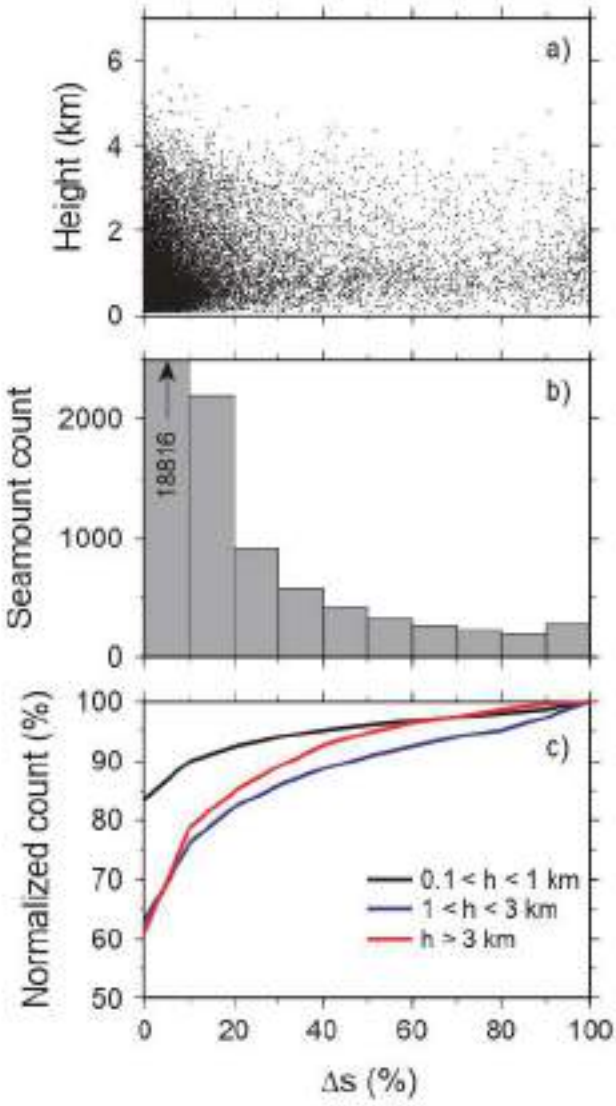

Figure 11. Bathymetric map coverage over potential seamounts. (a) Scatter plot of the bathymetric map coverage versus seamount height. (b) Histogram of bathymetric map coverage. Only 5828 potential seamounts have more than 10 per cent of their area mapped bathymetrically; 10 062 potential seamounts have not been mapped bathymetrically. (c) Normalized cumulative count of small (black), intermediate (blue), large (red) seamounts as a function of bathymetric map coverage. The count is normalized with respect to the total number of seamounts for each seamount group.

4 DISCUSSION

With different methodology and data, one will obtain dissimilar numbers of seamounts (Wessel 2001; Kitchingman & Lai 2004; Hillier & Watts 2007; Costello *et al.* 2010; Wessel *et al.* 2010); this makes it difficult to reconcile our results with published numbers. Using bathymetry, Hillier & Watts (2007) found 201 055 potential seamounts in the NGDC archieved single-beam ship bathymetry, while Kitchingman & Lai (2004) identified 14 287 potential seamounts in the ETOPO2 grid. In contrast, Wessel (2001) found 11 882 potential seamounts from the VGG 7.2 grid (recently revised from 14 675 after removing accidental duplicates, Wessel *et al.* 2010). One can also differentiate these numbers further based on size threshold, data resolution, methodologies, and other factors. Here, we will focus on two aspects of the broad definition of a seamount (Staudigel *et al.* 2010) that earlier studies did not consider. The first aspect is that a seamount is 'any geographically isolated topographic feature'. Previous studies commonly identified local summits on volcanic ridges as seamounts, but such ridges are geographically continuous. For example, we compare the potential seamounts from this study (KW; red dots) with those of Wessel (2001) (PW; yellow squares) in the eastern part of the Tuamotu Plateau (Fig. 12). Along the NW/SE-trending ridge (see A in Fig. 12), PW has multiple seamounts whereas KW has none after inspections (see crosses for the uninspected seamounts of KW). The second aspect is that seamounts are not 'features that are located on continental shelves or that are part of other major landmasses'. Because this geographical limitation was not imposed on the bathymetric studies (Kitchingman & Lai 2004; Hillier & Watts 2007), they found numerous seamounts along continental boundaries (e.g. within the Gulf of California). Thus, we can assume that any

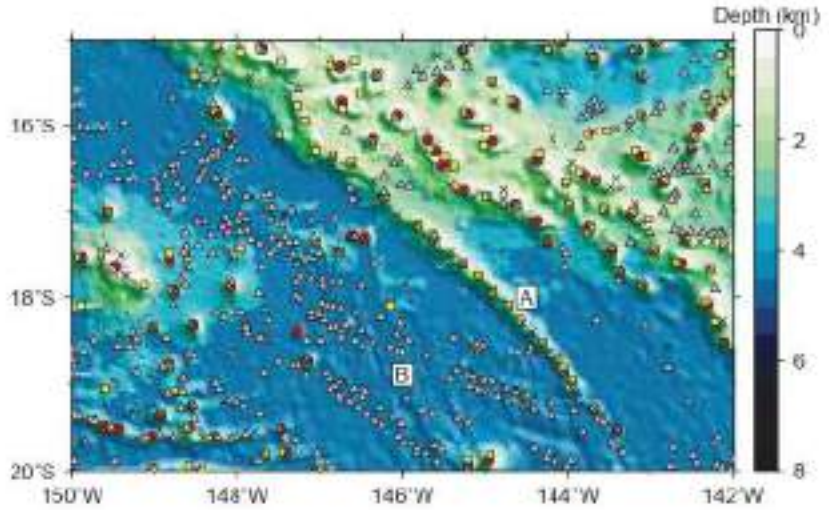

Figure 12. Comparison of potential seamounts identified by this study (red dots) with Wessel (2001) (yellow squares) and Hillier & Watts (2007) (grey triangles) near Tuamotu Plateau. Crosses indicate locations of unexpected potential seamounts in this study. The seamounts identified at the ridge (A) and along abyssal hills (B) biased the previous seamount counts.

potential seamount in these databases located too far from any of the KW seamounts is unlikely to be a seamount according to this new definition, which enables us to demonstrate how different and similar these databases are.

With this assumption, we make a first-order reconciliation of our results with the PW and HW (Hillier & Watts 2007) seamount databases by choosing any seamounts in the PW and HW databases that are within 5 km of any of the KW seamounts. This distance (5 km) is a conservative limit to allow for differences in the data used to search for seamounts. Our estimation shows that 5461 seamounts (~46 per cent) of the PW data and 4228 seamounts (~2 per cent) of the HW data are found within 5 km from the KW seamounts, while 2208 (~ 16 per cent) seamounts from the KL (Kitchingman & Lai 2004) data are within the reconciliation distance. For further comparison, we use the PW and HW data sets only because the KL data have the least number of reconciled seamounts.

The major difference between the PW and KW counts occurs for potential seamounts less than 3 km (Fig. 13a). This reduction is expected as the PW data have multiple seamounts on linear ridges (e.g. Fig. 12) and their predicted heights fall within that range ($1 < h < 3$ km). If the total volume of the non-reconcilable PW seamounts is linearly related with that of volcanic ridges, then the contribution of such ridges to intraplate volcanism can be significant because nearly half of the original PW seamounts are not found nearby the potential seamounts detected by our study. Thus, although we focus exclusively on seamounts in this study, the importance of volcanic ridges in understanding intraplate volcanism becomes self-evident. However, the reconciled PW data (PW | KW) still show many seamounts taller than 5 km, which KW does not have (Figs 13a). This means that the locations of these seamounts are close to each other except for the estimated heights, which leads to a further implication that these heights may be biased in some degree. The spatial distribution of these tall seamounts in the PW | KW data confirms that their heights are clearly overpredicted, because they would be islands in places where no islands exist (Fig. 14). Disregarding these seamounts makes the KW and PW | KW more comparable (see blue squares and red dots in Fig. 13a). The difference between the HW and KW counts, however, increases as the seamount height decreases (Fig. 13b). Although the general trend

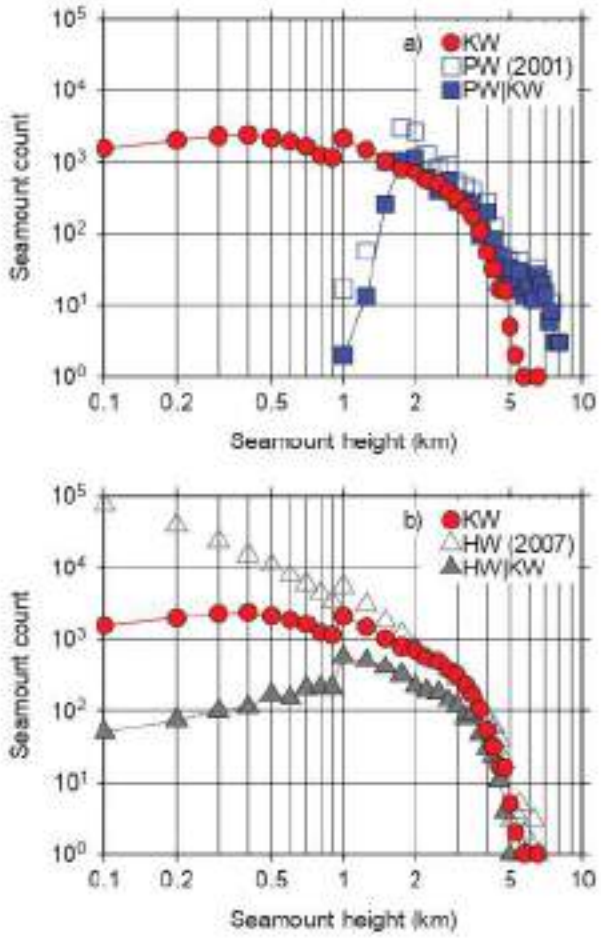

Figure 13. Height distribution of potential seamounts. (a) Log–log plot of the height distribution of potential seamounts from the KW (red dots), PW (blue open squares) and PW | KW (blue squares). (b) Log–log plot of the height distribution of potential seamounts from the KW, HW (grey open triangles), and HW | KW (grey triangles).

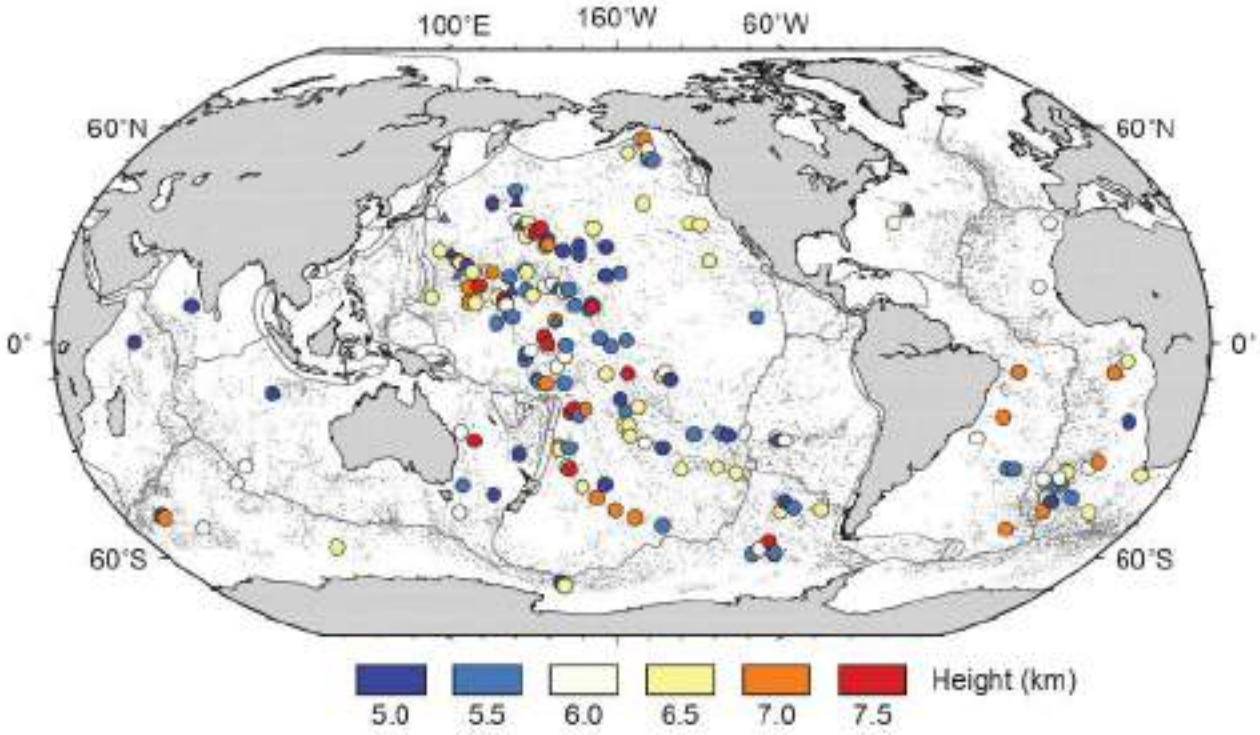

Figure 14. Spatial distribution of the PW | KW potential seamounts of $h > 5$ km in Figure 13. According to the predicted heights of these seamounts, we should see islands (circles) at places where such features cannot be found (e.g. Southeast Indian Ridge). Only a few of the large PW | KW seamounts are barely submerged (triangles). This clearly indicates that their heights are overestimated. The black dots are the KW potential seamounts.

of the height distribution is similar to KW, the HW | KW has much fewer seamounts (especially at $1 < h < 3$ km) because of the sparse ship tracks (see grey triangles and red dots in Fig. 13b). Taking into account the overestimated heights of the PW | KW data and the incomplete ship-track coverage of the HW | KW data, the similarity of all three seamount databases within $1 < h < 6$ km is noteworthy in light of the different data sets and methods used by these studies.

For the small seamounts (<1 km), however, no general trend is observed as both the HW and HW | KW counts diverge from KW (Fig. 13b). The direct comparison between KW and HW (see red dots and grey triangles in Fig. 12) implies that HW identified abyssal hills (see B in Fig. 12) as seamounts because their height and length scales increasingly overlap with those of abyssal hills; furthermore, seamounts and abyssal hills are difficult to differentiate in 1-D profiles. In addition, it implies that the HW missed many small seamounts that we have detected. Thus, the HW count for the small seamounts becomes questionable.

The gravity anomalies over the small seamounts can be ambiguous due to upward continuation, data resolution, altimetry noise level, seafloor roughness and sediment cover (Wessel *et al.* 2010). In order to assess these effects on finding seamounts from altimetry-based gravity data, we define the 'detectability' of a seamount for a given depth and height by considering possible scenarios; the details are included in Appendix. Fig. 15 compares the four detectability zones and the seamount population found by this study (yellow dots). The majority of the potential seamounts are situated at 3–6 km depth. Seamounts deeper than 6 km were detected near subduction zones. About 35 per cent of the potential seamounts are inside the red zone (i.e. null detectability zone), although the seamount models that have VGG amplitudes less than the given threshold (10 Eötvös) define this zone. Yet, contouring and the automatic inspection ensured that all the identified seamounts have VGG amplitudes larger than this threshold. This mismatch implies that the detectability model underpredicts VGG due to the neglected non-linear (i.e. higher order) terms of bathymetry, fixed ratio between height and radius, difference in the distributed mass between elliptical and circular cones, and fixed truncation ratio. In addition, the heights of the potential seamounts were obtained from the predicted depth grid (Smith & Sandwell 1997), which could severely underestimate the actual heights of smaller seamounts. The VGG anomaly, thus, is large enough to be confidently identified as seamounts but the predicted bathymetry can be too small. Despite the gap between the real data and simplified detectability model, the many potential seamounts inside the red zone are still questionable (especially the small, deep ones) and may require ship bathymetry for confirmation.

5 CONCLUSIONS

For a global seamount analysis, we have developed a non-linear inversion method to search for potential seamounts in the satellite-derived VGG grid. An elliptical polynomial model was applied to approximate VGG anomalies due to seamounts. In addition, the statistical significance of each potential seamount was examined using two model selection criteria, which considered the correlated nature of the gravity data. After making both automatic and manual inspections of potential seamounts determined by the inversion process, we isolated 24 643 seamounts with $h \geq 0.1$ km globally. In this count, the number of the small seamounts ($h < 1$ km) is about twice that of the intermediate and large seamounts ($h \geq 1$ km). The small seamounts are mostly found on the young seafloor and their counts decrease exponentially for old seafloor. This suggests our count

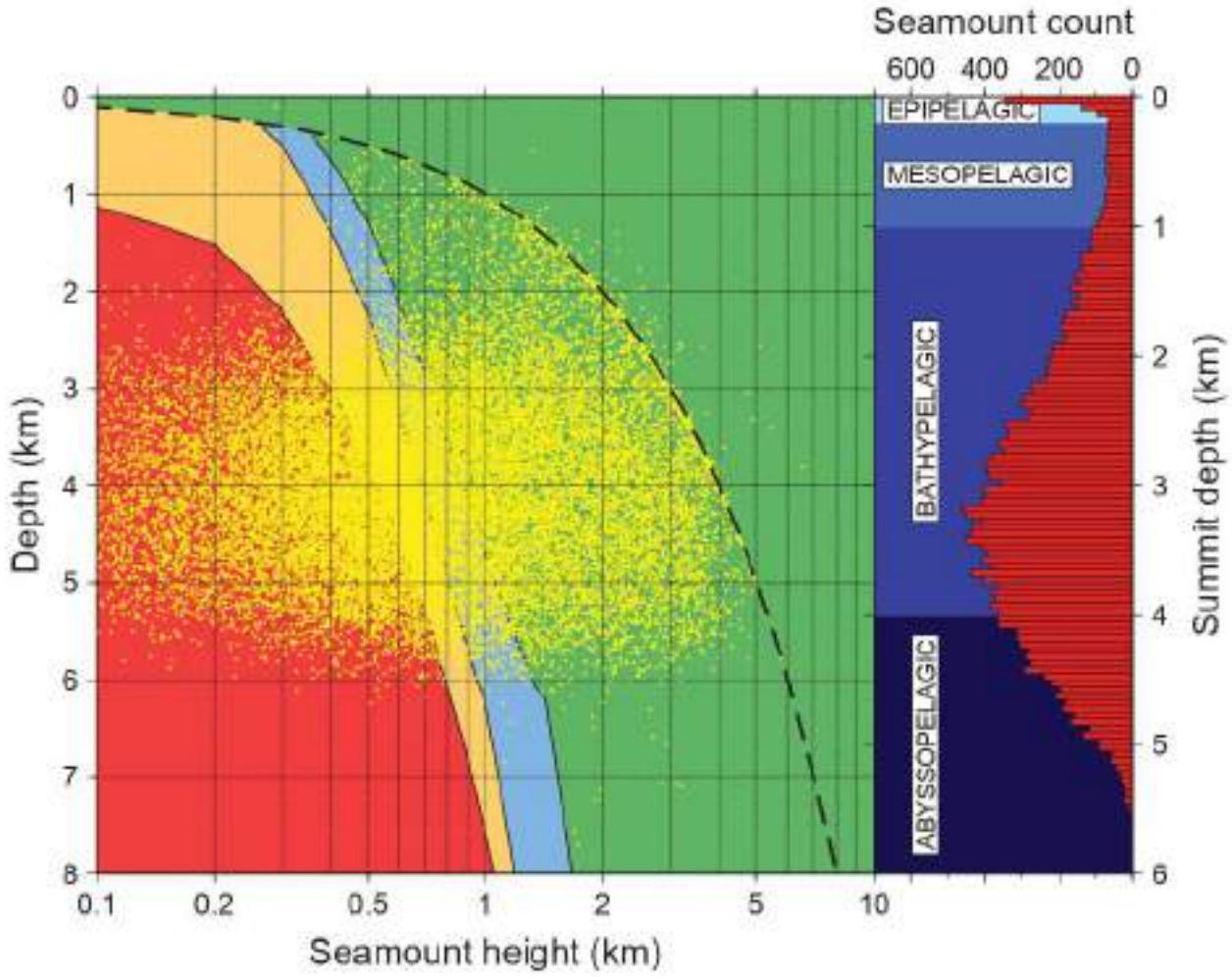

Figure 15. Modelled detectability zones for seamounts using VGG data. Each zone is based on maximum VGG amplitudes that reflect changes in seamount height, regional depth, density of seamount and sediment, thickness of sediment cover and different noise level (see Appendix for details). Seamounts in the green zone should be easily detected, whereas those in the red zone are problematic as they are too small for the given depths. Seamounts in intermediate zones (blue and orange) can be identifiable using robust methodology or better data. Yellow dots are the estimated heights from this study. The histogram of summit depths interestingly follows a normal distribution centred on ~3-km depth and illustrates that seamounts have the potential to sustain epipelagic and mesopelagic environments crucial for marine animals. The dashed line denotes a boundary between islands and seamounts. Modified from Wessel *et al.* (2010).

for the small seamounts is fundamentally limited due to attenuated gravity signals of small seamounts in deep-ocean settings (i.e. upward continuation). Because the size-frequency distribution does not follow commonly used statistical models, we have assumed a constant production of small seamounts in a near-ridge environment and estimated a new census of global seamounts ($h \geq 0.1$ km) that ranges from 40 000 to 55 000. Our new global seamount count is not significantly increased from the previous counts despite improved resolution of the VGG grid and a better methodology to characterize seamounts. On the other hand, comparison of our seamount data with the previous global studies has demonstrated that the previous counts were inflated by including ridges and abyssal hills as seamounts. The seamount data from this study are accessible from http://www.soest.hawaii.edu/PT/SMTS.

ACKNOWLEDGMENTS

This study was supported by NSF grant OCE-0526496, and the University of Hawaii at Manoa (SSK) through Maui High Performance Computing Center (MHPCC) Student Engagement Grant, Graduate Student Organization Grant, and Fred M. Bullard Fellowship. This paper was completed with the help of the Korea government through MEST grant 2009-0092790 (SSK). We thank M. Diament the Editor and two anonymous reviewers for the constructive comments that improved this manuscript greatly. This is SOEST contribution 8200.

REFERENCES

Abers, G.A., Parsons, B. & Wessel, J.K., 1988. Seamount abundance and distributions in the southeast Pacific, *Earth planet. Sci. Lett.*, **87**, 137–151.

Andersen, O.B. & Knudsen, P., 1998. Global marine gravity field from the ERS-1 and Geosat geodetic mission altimetry, *J. geophys. Res.*, **103**, 8129–8137.

Andersen, O.B., Knudsen, P. & Berry, P.A.M., 2010. The DNSC08GRA global marine gravity field from double retracked satellite altimetry, *J. Geodyn.*, **84**, 191–199.

Baptista, E.C., Balbi, E.A. & da Costa, G.R.M., 2005. Logarithmic barrier-augmented Lagrangian function to the optimal power flow problem, *Electr. Power Energy Syst.*, **27**, 528–532.

Batiza, R., 1982. Abundances, distribution and sizes of volcanoes in the Pacific Ocean and implications for the origin of non-hotspot volcanoes, *Earth planet. Sci. Lett.*, **60**, 195–206.

Batiza, R. & Vanko, D., 1983. Volcanic development of small oceanic central volcanoes on the flanks of the East Pacific Rise inferred from narrow-beam echo-sounder surveys, *Mar. Geol.*, **54**, 53–90.

Baudry, N. & Calmant, S., 1991. 3-D modelling of seamount topography from satellite altimetry, *Geophys. Res. Lett.*, **18**, 1143–1149.

Baudry, N., Dismont, M. & Albouy, Y., 1987. Precise location of unsurveyed seamounts in the Austral archipelago area using SEASAT data, *Geophys. J. R. astr. Soc.*, **89**, 869–888.

BBC, 2005. Crew blamed for grounding US sub, http://news.bbc.co.uk/2/hi/americas/4527459.stm (last accessed 2010 July 17).

Becker, J.J. *et al.*, 2009. Global bathymetry and elevation data at 30 arc seconds resolution: SRTM30_PLUS, *Mar. Geod.*, **32**, 355–371.

Behn, M.D., Sinton, J.M. & Detrick, R.S., 2004. Effect of the Galápagos hotspot on seafloor volcanism along the Galápagos Spreading Center (90.9–97.6°W), *Earth planet. Sci. Lett.*, **217**, 331–347.

Bird, P., 2003. An updated digital model of plate boundaries, *Geochem. Geophys. Geosyst.*, **4**, 1027, doi:10.1029/2001GC000252.

Blakely, R.J., 1996. *Potential Theory in Gravity and Magnetics Applications*, 1 edn, Cambridge Univ. Press, Cambridge, UK.

Calmant, S., 1994. Seamount topography by least-squares inversion of altimetric geoid heights and shipborne profiles of bathymetry and/or gravity anomalies, *Geophys. J. Int.*, **119**, 428–452.

Calmant, S. & Baudry, N., 1996. Modelling bathymetry by inverting satellite altimetry data: a review, *Mar. geophys. Res.*, **18**, 123–134.

Cazenave, A., Lago, B. & Dominh, K., 1983. Thermal parameters of the oceanic lithosphere estimated from geoid height data, *J. geophys. Res.*, **88**, 1105–1118.

Chandler, M.T. & Wessel, P., 2008. Improving the quality of marine geophysical track line data: along-track analysis, *J. geophys. Res.*, **113**, B02102, doi:10.1029/2007JB005051.

Clark, M.R. *et al.*, 2010. The ecology of seamounts: structure, function, and human impacts, *Annu. Rev. Mar. Sci.*, **2**, 253–278.

Costello, M.J., Cheung, A. & Hauwere, N.D., 2010. Surface area and the seabed area, volume, depth, slope, and topographic variation for the world's seas, oceans, and countries, *Environ. Sci. Technol.*, **44**, 8821–8828.

Craig, C.H. & Sandwell, D.T., 1988. Global distribution of seamounts from Seasat profiles, *J. geophys. Res.*, **93**, 10 408–410 420.

Dettmer, J., 2006. Geoacoustic reflectivity inversion: a Bayesian approach, *PhD thesis*, University of Victoria.

Divins, D.L., 2009. NGDC total sediment thickness of the world's oceans & marginal seas, *available at* http://www.ngdc.noaa.gov/mgg/sedthick/sedthick.html (last accessed 2009 December).

Dixon, T.H., Naraghi, M., McNutt, M.K. & Smith, S.M., 1983. Bathymetric prediction from SEASAT altimeter data, *J. geophys. Res.*, **88**, 1563–1571.

Dixon, T.H. & Parke, M.E., 1983. Bathymetry estimates in the southern oceans from Seasat altimetry, *Nature*, **304**, 406–411.

Dosso, S.E., Nielsen, P.L. & Wilmut, M.J., 2006. Data error covariance in matched-field geoacoustic inversion, *J. acous. Soc. Am.*, **119**, 208–219.

Fornari, D.J., Perfit, M.R., Allan, J.F. & Batiza, R., 1988. Small-scale heterogeneities in depleted mantle sources: near-ridge seamount lava geochemistry and implications for mid-ocean-ridge magmatic processes, *Nature*, **331**, 511–513.

Friedrich, G. & Schmitz-Wiechowski, A., 1980. Mineralogy and chemistry of a ferromanganese crust from a deep-sea hill, Central Pacific, 'Valdivia' Cruise 13/2, *Mar. Geol.*, **37**, 71–90.

Gille, S.T., Metzger, E.J. & Tokmakian, R., 2004. Seafloor topography and ocean circulation, *Oceanography*, **17**, 47–54.

Grigg, R.W., Malahoff, A., Chave, E.H. & Landahl, J., 1987. Seamount benthic ecology and potential environmental impact from manganese crust mining in Hawaii, in *Seamounts, Islands, and Atolls*, pp. 379–390, eds Keating, B.H., Fryer, P., Batiza, R. & Boehlert, G.W., AGU Washington, DC.

Haxby, W.F., Karner, G.D., LaBrecque, J.L. & Weissel, J.K., 1983. Digital images of combined oceanic and continental data sets and their use in tectonic studies, *EOS, Trans. Am. geophys. Un.*, **64**, 995–1004.

Haxby, W.F. & Weissel, J.K., 1986. Evidence for small-scale mantle convection from Seasat altimeter data, *J. geophys. Res.*, **91**, 3507–3520.

Hillier, J.K., 2007. Pacific seamount volcanism in space and time, *Geophys. J. Int.*, **168**, 877–889.

Hillier, J.K. & Watts, A.B., 2007. Global distribution of seamounts from ship-track bathymetry data, *Geophys. Res. Lett.*, **34**, L13304, doi:10.1029/2007GL029874.

Jarrard, R.D. & Clague, D.A., 1977. Implications of Pacific islands and seamount ages for the origins of volcanic chains, *Rev. Geophys.*, **15**, 57–76.

Jordan, T.H., Menard, H.W. & Smith, D.K., 1983. Density and size distribution of seamounts in the eastern Pacific inferred from wide-beam sounding data, *J. geophys. Res.*, **88**, 10 508–10 518.

Jung, W.-Y. & Vogt, P.R., 1992. Predicting bathymetry from Geosat-ERM and shipborne profiles in the South Atlantic Ocean, *Tectonophysics*, **210**, 235–253.

Kim, S.-S. & Wessel, P., 2010. Flexure modelling at seamounts with dense cores, *Geophys. J. Int.*, **182**, 583–598.

Kitchingman, A. & Lai, S., 2004. Inferences of potential seamount locations from mid-resolution bathymetric data, in *Seamounts: Biodiversity and Fisheries*, pp. 7–12, eds Morato, T. & Pauly, D., Fisheries Centre Research Reports.

Lazarewicz, A.P. & Schwank, D.C., 1982. Detection of uncharted seamounts using satellite altimetry, *Geophys. Res. Lett.*, **9**, 385–388.

Li, Y. & Oldenburg, D.W., 1996. 3-D inversion of magnetic data, *Geophysics*, **61**, 394–408.

Mammericks, J., 1992. The Foundation seamounts: tectonic setting of a newly discovered seamount chain in the south Pacific, *Earth planet. Sci. Lett.*, **113**, 293–306.

Marks, K.M., 1996. Resolution of the Scripps/NOAA marine gravity field from satellite altimetry, *Geophys. Res. Lett.*, **23**, 2069–2072.

Maus, S., Green, C.M. & Fairhead, J.D., 1998. Improved ocean-geoid resolution from retracked ERS-1 satellite altimeter waveforms, *Geophys. J. Int.*, **134**, 243–253.

McAdoo, D.C. & Marks, K.M., 1992. Gravity fields of the Southern Ocean from Geosat data, *J. geophys. Res.*, **97**, 3247–3260.

McAdoo, D.C. & Sandwell, D.T., 1989. On the source of crossgrain lineations in the central Pacific gravity field, *J. geophys. Res.*, **94**, 9341–9352.

McNutt, M.K., 1998. Superswells, *Rev. Geophys.*, **36**, 211–244.

Menard, H.W., 1964. *Marine Geology of the Pacific*, McGraw-Hill, New York.

Mitchell, N.C., 2001. Transition from circular to stellate forms of submarine volcanoes, *J. geophys. Res.*, **106**, 1987–2003.

Mofjeld, H.O., Symons, C.M., Lonsdale, P., Gonzalez, F.I. & Titov, V.V., 2004. Tsunami scattering and earthquake faults in the deep Pacific ocean, *Oceanography*, **17**, 38–46.

Montgomery, D.C. & Peck, E.A., 1992. *Introduction to Linear Regression Analysis*, Wiley, New York.

Müller, R.D., Sdrolias, M., Gaina, C. & Roest, W.R., 2008. Age, spreading rates, and spreading asymmetry of the world's ocean crust, *Geochem. Geophys. Geosyst.*, **9**, Q04006, doi:10.1029/2007GC001743.

NGDC, 2006. *2-minute Gridded Global Relief Data (ETOPO2v2)* National Oceanic and Atmospheric Administration, *available at:* http://www.ngdc.noaa.gov/mgg/fliers/06mgg01.html (last accessed 2006 November 5).

Parker, R.L., 1972. The rapid calculation of potential anomalies, *Geophys. J. R. astr. Soc.*, **31**, 447–455.

Parsons, B. & Sclater, J.G., 1977. An analysis of the variation of ocean floor bathymetry and heat flow with age, *J. geophys. Res.*, **82**, 803–827.

Pitcher, T.J., Morato, T., Hart, P.J.B., Clark, M., Haggan, N. & Santos, R.S., 2007. *Seamounts: Ecology, Fisheries & Conservation*, Wiley-Blackwell, Oxford.

Press, W.H., Teukolsky, S.A., Vetterling, W.T. & Flannery, B.P., 1992. *Numerical Recipes in C: The Art of Scientific Computing*, 2nd edn, Cambridge Univ. Press, Cambridge.

Ramillien, G. & Cazenave, A., 1997. Global bathymetry derived from altimeter data of the ERS-1 geodetic mission, *J. Geodyn.*, **23**, 129–149.
Ramillien, G. & Wright, I.C., 2000. Predicted seafloor topography of the New Zealand region: a nonlinear least squares inversion of satellite altimetry data, *J. geophys. Res.*, **105**, 16 577–16 590.
Rappaport, Y., Nasr, D.F., Barton, C.C., Liu, Z.J. & Hey, R.N., 1997. Morphology and distribution of seamounts surrounding Easter Island, *J. geophys. Res.*, **102**, 24 713–24 728.
Ribe, N.M., 1982. On the interpretation of frequency response functions for oceanic gravity and bathymetry, *Geophys. J. R. astr. Soc.*, **70**, 273–294.
Sandwell, D.T. & Smith, W.H.F., 1997. Marine gravity anomaly from Geosat and ERS-1 satellite altimetry, *J. geophys. Res.*, **102**, 10 039–10 054.
Sandwell, D.T. & Smith, W.H.F., 2005. Retracking ERS-1 altimeter waveforms for optimal gravity field recovery, *Geophys. J. Int.*, **163**, 79–89.
Sandwell, D.T. & Smith, W.H.F., 2009. Global marine gravity from retracked Geosat and ERS-1 altimetry: ridge segmentation versus spreading rate, *J. geophys. Res.*, **114**, B01411, doi:10.1029/2008JB006008.
Sandwell, D.T. & Wessel, P., 2010. Box 3: seamount discovery tool aids navigation to uncharted seafloor features, *Oceanography*, **23**, 34–36.
Sichoix, L. & Bonneville, A., 1996. Prediction of bathymetry in French Polynesia constrained by shipboard data, *Geophys. Res. Lett.*, **23**, 2469–2472.
Small, C. & Sandwell, D.T., 1994. Imaging mid-ocean ridge transitions with satellite gravity, *Geology*, **22**, 123–126.
Smith, D.K. & Cann, J.R., 1990. Hundreds of small volcanoes on the median valley floor of the Mid-Atlantic Ridge at 24–30° N, *Nature*, **348**, 152–155.
Smith, W.H.F., 1990. Marine geophysical studies of seamounts in the Pacific Ocean basin, *PhD thesis*, Columbia Univ.
Smith, W.H.F. & Sandwell, D.T., 1994. Bathymetric prediction from dense satellite altimetry and sparse shipboard bathymetry, *J. geophys. Res.*, **99**, 21 803–21 824.
Smith, W.H.F. & Sandwell, D.T., 1997. Global sea floor topography from satellite altimetry and ship depth soundings, *Science*, **277**, 1956–1962.
Smoot, N.C., 1982. Guyots of the Mid-Emperor Chain mapped with multibeam sonar, *Mar. Geol.*, **47**, 153–163.
Staudigel, H., Koppers, A.A.P., Lavelle, J.W., Pitcher, T.J. & Shank, T.M., 2010. Box 1: defining the word "seamount", *Oceanography*, **23**, 20–21.
Stein, S. & Gordon, R.G., 1984. Statistical tests of additional plate boundaries from plate motion inversions, *Earth planet. Sci. Lett.*, **69**, 401–412.
Tsai, C.-L. & McQuarrie, A.D.R., 1999. *Regression and Time Series Model Selection*, 1st edn, World Scientific Publishing Co., Singapore.
Vogt, P.R. & Jung, W.-Y., 2000. GCMaP: a matchless resolution to start the new millennium, *EOS, Trans. Am. geophys. Un.*, **81**, 254, 258.
Watts, A.B. & Ribe, N.M., 1984. On geoid heights and flexure of the lithosphere at seamounts, *J. geophys. Res.*, **89**, 11 152–11 170.
Watts, A.B., Sandwell, D.T., Smith, W.H.F. & Wessel, P., 2006. Global gravity, bathymetry, and the distribution of submarine volcanism through space and time, *J. geophys. Res.*, **111**, B08408, doi:10.1029/2005JB004083.
Wessel, P., 2001. Global distribution of seamounts inferred from gridded Geosat/ERS-1 altimetry, *J. geophys. Res.*, **106**, 19 431–19 441.
Wessel, P. & Chandler, M.T., 2011. The spatial and temporal distribution of marine geophysical surveys, *Acta Geophys.*, **59**, 55–71.
Wessel, P. & Kroenke, L.W., 1997. Relocating Pacific hotspots and refining absolute plate motions using a new geometric technique, *Nature*, **387**, 365–369.
Wessel, P. & Lyons, S., 1997. Distribution of large Pacific seamounts from Geosat/ERS-1: implications for the history of intraplate volcanism, *J. geophys. Res.*, **102**, 22 459–22 476.
Wessel, P., Sandwell, D.T. & Kim, S.-S., 2010. The global seamount census, *Oceanography*, **23**, 24–33.
White, J.V., Sailor, R.V., Lazewicz, A.R. & LeSchack, A.R., 1983. Detection of seamount signatures in SEASAT altimeter data using matched filters, *J. geophys. Res.*, **88**, 1541–1551.

APPENDIX

The gravity signals over small seamounts (< 1 km) can become ambiguous because of upward continuation, data resolution, altimetry noise level, seafloor roughness, and sediment cover (Wessel *et al.* 2010). Because these are the main parameters that determine the maximum VGG amplitude of a seamount, we predicted VGG amplitudes for various cases by changing these parameters and defined the 'detectability' of a seamount for a given depth and height by examining if its VGG amplitude exceeded a prescribed threshold (Wessel *et al.* 2010). A truncated circular cone model was used to approximate the typical topography of seamounts, with basal radius of 4.5 times the height and a fixed truncation ratio of 0.31 (Wessel 2001). As more than 60 per cent of the seafloor has less than 200 m of sediments (Wessel *et al.* 2010), we assigned upper and lower limits on sediment thickness for the oldest seafloor (i.e. 180 Ma) of 600 and 300 m, respectively. Sediment thickness, then, was linearly interpolated to the ridges (i.e. 0 Ma), which enabled us to relate sediment thickness to predicted depth of the seafloor formed at a given age (Parsons & Sclater 1977). By equating the predicted depth to the regional depth for a given seamount, we could examine the three cases of no sediments, minimum and maximum sediment thicknesses. In addition, we applied a second-order, low-pass Butterworth filter with a cut-off wavelength of 18 km to the predicted VGG signals (e.g. Marks 1996) and kept only the linear term due to bathymetry (Parker 1972). By considering different scenarios using these constraints, we arrived at four 'detectability zones' for seamounts (Fig. 15). The high detectability zone (green domain) encloses seamounts exhibiting VGG amplitudes above the higher threshold (15 Eötvös), even when the maximum sediment thickness and the least density contrast between seamount (2500 kg m^{-3}) and sediment (2300 kg m^{-3}) were considered. In this zone, gravity over seamounts is easily distinguishable from gravity due to abyssal hills and data noise. The intermediate detectability zone (blue domain) represents seamounts having predicted VGG amplitudes above the lower threshold (10 Eötvös) when the minimum sediment thickness and the largest density contrast between seamount (2800 kg m^{-3}) and sediment (2000 kg m^{-3}) were considered. The low detectability zone (orange domain) encompasses seamounts with VGG amplitudes above the lower threshold when the less-dense seamount (2500 kg m^{-3}) and no sediment cover were considered. Finally, the null detectability zone (red domain) groups seamounts having VGG amplitudes less than the lower threshold because of upward continuation alone; the boundary between the orange and red domains was obtained without the low-pass filter.